Modelling smooth- and transitionally rough-wall turbulent channel flow by leveraging inner–outer interactions and principal component analysis

Sicong Wu[1,†], **Kenneth T. Christensen**[2,3] **and Carlos Pantano**[1]

[1]Department of Mechanical Science and Engineering, University of Illinois at Urbana-Champaign, Urbana, IL 61801, USA

[2]Department of Aerospace and Mechanical Engineering and Civil and Environmental Engineering and Earth Sciences, University of Notre Dame, Notre Dame, IN 46556, USA

[3]International Institute for Carbon Neutral Energy Research (WPI-I2CNER), Kyushu University, Fukuoka 819-0385, Japan

Direct numerical simulations (DNS) of turbulent channel flow over rough surfaces, formed from hexagonally packed arrays of hemispheres on both walls, were performed at friction Reynolds numbers $Re_\tau = 200$, 400 and 600. The inner normalized roughness height $k^+ = 20$ was maintained for all Reynolds numbers, meaning all flows were classified as transitionally rough. The spacing between hemispheres was varied within $d/k = 2$–4. The statistical properties of the rough-wall flows were contrasted against a complementary smooth-wall DNS at $Re_\tau = 400$ and literature data at $Re_\tau = 2003$ revealing strong modifications of the near-wall turbulence, although the outer-layer structure was found to be qualitatively consistent with smooth-wall flow. Amplitude modulation (AM) analysis was used to explore the degree of interaction between the flow in the roughness sublayer and that of the outer layer utilizing all velocity components. This analysis revealed stronger modulation effects, compared to smooth-wall flow, on the near-wall small-scale fluctuations by the larger-scale structures residing in the outer layer irrespective of roughness arrangement and Reynolds number. A predictive inner–outer model based on these interactions, and exploiting principal component analysis (PCA), was developed to predict the statistics of higher-order moments of all velocity fluctuations, thus addressing modelling of anisotropic effects introduced by roughness. The results show excellent agreement between the predicted near-wall statistics up to fourth-order moments compared to the original statistics from the DNS, which highlights the utility of the PCA-enhanced AM model in generating physics-based predictions in both smooth- and rough-wall turbulence.

Key words: turbulence modelling, turbulence simulation, turbulent boundary layers

† Email address for correspondence: swu52@illinois.edu

1. Introduction

Turbulent flows over rough surfaces are encountered in many industrial and natural situations, for which substantial variation in the topographical complexity of the roughness often exists. Examples include degraded surfaces of turbine blades (Bons *et al.* 2001), ice accumulation on aircraft wings (Bragg, Broeren & Blumenthal 2005) and ablation of vehicle surfaces during atmospheric re-entry (Vignoles *et al.* 2009), to name a few. Similar topographical complexity exists in meteorological boundary layers, where experimental investigations have been focused on flows over vegetation canopies, rural terrains and urban cities (see Monin 1970; Cheng & Castro 2002). Understanding turbulence interactions in this context also contributes to our understanding of global biogeochemical cycles (Finnigan 2000), for example.

Though the complexity of the roughness morphology in laboratory studies is often greatly reduced and well controlled (periodic arrays of hemispheres, pyramids, etc.), compared to realistic roughness topographies, such studies of simplified topographies will inevitably encounter unavoidable difficulties in accessing the flow structure in the immediate vicinity of the roughness (Flack, Schultz & Shapiro 2005; Wu & Christensen 2007; Hong, Katz & Schultz 2011; Barros & Christensen 2014, among others). For example, Raupach, Antonia & Rajagopalan (1991) pointed out that a conventional hot-wire probe suffers from a limited velocity-vector acceptance angle and spatial resolution in measuring high-intensity turbulence within the roughness sublayer, which adversely impacts the accuracy of measured shear stress just above the roughness crest.

Optical techniques, such as laser Doppler velocimetry and particle image velocimetry (PIV), circumvent these difficulties to some degree; however, their reliance on the use of high-power lasers to illuminate tracer particles in the flow inevitably leads to laser light reflections from the solid surface which corrupts such measurements in the immediate vicinity of even idealized roughness elements. Furthermore, such measurements cannot access the flow below the roughness crests due to similar difficulties, nor can they fully access the spatio-temporal character of this unsteady, three-dimensional (3-D) turbulent scenario. Recent PIV studies meant to characterize the turbulence in the roughness sublayer of flow over a realistic roughness topography replicated from a damaged turbine blade clearly illustrate the limitations of optical measurements near complex surfaces (Wu & Christensen 2007, 2010; Mejia-Alvarez & Christensen 2010, 2013; Barros & Christensen 2014). While the flow in the outer portion of the roughness sublayer was well characterized in these efforts, the flow within 1–2 roughness heights of the topography could not be interrogated owing to laser reflections from the multi-scale roughness topography. These inherent measurement challenges have inhibited advance our understanding of roughness-sublayer physics and thus in the development of near-wall models for the accurate simulation of practical rough-wall flows.

With the advance of computational power over the last decades, it is now practical to carry out direct numerical simulations (DNS) of smooth wall-bounded turbulence with increasingly higher Reynolds numbers (*Re*) (Kim, Moin & Moser 1987; Hoyas & Jiménez 2008; Lee & Moser 2015). DNS of rough-wall flows with even idealized geometric features have the advantage of fully resolving flow physics from the largest to the smallest relevant spatial and temporal scales. Examples include DNS of channel flows over sandpaper (Scotti 2006; Yuan & Piomelli 2014), triangular riblets (Choi, Moin & Kim 1993; Chu & Karniadakis 1993), wavy walls (De Angelis, Lombardi & Banerjee 1997), arrays of 2-D rods (Ashrafian, Andersson & Manhart 2004; Lee, Sung & Krogstad 2011) or square bars (Krogstad *et al.* 2005; Ikeda & Durbin 2007; Burattini, Leonardi & Orlandi 2008; Orlandi & Leonardi 2008) and 3-D arrays of

cubes (Coceal *et al.* 2007; Lee & Sung 2007; Leonardi & Castro 2010), hemispheres (Chatzikyriakou *et al.* 2015) or spheres (Chan-Braun, García-Villalba & Uhlmann 2011; Ghodke & Apte 2016), etc. More recently, DNS of flow over realistic roughness have also been considered despite the topographical complexity (Busse, Lutzner & Sandham 2015; Busse, Thakkar & Sandham 2017, for example).

With regard to rough-wall flow physics, it is well established that the presence of either 3-D or 2-D transverse idealized roughness elements (Ashrafian *et al.* 2004; Nagano, Hattori & Houra 2004; Coceal *et al.* 2007) increases the drag at the wall (except in the case of flow-aligned riblets for which a reduction of drag is observed (Choi *et al.* 1993; Chu & Karniadakis 1993; Orlandi, Leonardi & Antonia 2006)). A downward shift of the mean velocity profile compared to smooth-wall flow is one consequence of this increased surface drag and is termed the roughness function ΔU^+ (where '+' indicates normalization in inner units), which generally varies with the flow geometry, the characteristics of the topography and Re. The roughness type can be classified based on the behaviour of ΔU^+ with respect to Re and/or geometrical characteristics of the roughness. A 'k-type' roughness refers to one in which ΔU^+ depends on the roughness height and Re. A 'd-type' roughness depends on the outer length scale, such as the diameter of the pipe, the thickness of a boundary layer or the half-width of the channel (Perry, Schofield & Joubert 1969). Other roughness parameters, such as the packing density, aspect ratio, higher-order statistics of the roughness (skewness, flatness), etc. may also be relevant in characterizing the dynamics of rough-wall flow; however, a more complete parameterization of roughness effects in this regard remains an open topic of research.

Recent smooth-wall turbulence studies highlight that physics-based predictions of the flow require a comprehensive understanding of the interactions or coupling between the outer flow and the flow in the near-wall region. Recently, Marusic, Mathis & Hutchins (2010) developed an amplitude modulation (AM) analysis to quantify such effects in smooth-wall turbulent boundary layers at high Re and found many statistical details that connect the outer flow structure with that of the near-wall region using single-point measurements of streamwise velocity. In particular, they reported a clear AM effect of the large-scale structures imparted on the small-scale near-wall turbulence, with the effect growing with Re (Hutchins & Marusic 2007*a*,*b*). This growth of the AM effect with Re is also apparent in a suite of DNS of a compressible, developing smooth-wall turbulent boundary layer for $205 < Re_\tau < 1123$ reported by Bernardini & Pirozzoli (2011). Leveraging the 3-D spatially resolved data afforded by DNS, compared to the single-point measurements in experiments, Bernardini & Pirozzoli (2011) computed true two-point AM correlation coefficients as a function of the wall-normal position and found that AM effects begin to develop at approximately $Re_\tau = 400$ where symmetry is broken in the correlation and a secondary, off-diagonal peak forms which they argue is the onset of nonlinear AM phenomena of the outer large-scale structures on the smaller scales in the near-wall region. Similarly, Pathikonda & Christensen (2017*b*) leveraged spatially resolved particle image velocimetry data acquired in a smooth-wall turbulent boundary layer to compute two-point AM correlations and identified distinct off-diagonal AM signatures that cannot be found in single-point measurements. Finally, Mathis, Hutchins & Marusic (2011) also developed an inner–outer predictive model that connects the large-scale behaviour in the logarithmic region to the near-wall flow features. This was possible owing to the discovery of an almost universal signal that was extracted from a calibration process based on AM analysis. Mathis *et al.* (2011) used this framework to successfully predict the statistics of u' up to the sixth-order moment

and showed excellent agreement with experimental data over a wide range of *Re*. More recently, Mathis *et al.* (2013) applied this method to predict characteristics of the wall shear stress in smooth-wall flows.

A similar connection may be present in rough-wall turbulence as the outer region of the flow often exhibits outer-layer similarity (Townsend 1976) to smooth-wall flow when the roughness height is small compared to the outer length scale (meaning that the wall shear stress and outer length scale adapt to the roughness in a universal manner) (Raupach *et al.* 1991; Flack *et al.* 2005; Wu & Christensen 2007, among others). This similarity exists not only for basic statistics of the flow, but also for the overall spatial structure of the larger-scale motions that occupy the outer region (Volino, Schultz & Flack 2007; Wu & Christensen 2010; Birch & Morrison 2011; Mejia-Alvarez, Wu & Christensen 2014, for example). Anderson (2016) utilized large-eddy simulations (LES) of turbulence overlying cube roughness to study the existence of AM effects in this rough-wall flow and reported enhanced AM effects compared to smooth-wall flow. Squire *et al.* (2016) conducted two-probe hot-wire measurements similar to those of Marusic *et al.* (2010) but for rough-wall flow and similarly reported an enhanced AM effect coupled with a reduced superposition effect. Finally, Pathikonda & Christensen (2017*a*) conducted two-probe hot-wire measurements in flow over the realistic roughness topography studied by Wu & Christensen (2007, 2010) and Mejia-Alvarez & Christensen (2013), Mejia-Alvarez *et al.* (2014) and found a similar enhancement of the AM effect, although the degree of enhancement was found to depend upon spanwise location relative to the irregular roughness features as this type of roughness induces the formation of turbulent secondary flows which lead to spanwise heterogeneity in the flow itself (Barros & Christensen 2014; Willingham *et al.* 2014; Anderson, Barros & Christensen 2015).

With this background in mind, this study explores the existence of AM effects in rough-wall turbulent channel flow using state-of-the-art fully roughness-resolving DNS for $200 < Re_\tau < 600$. A complementary DNS of smooth-wall turbulent channel flow at $Re_\tau = 400$ was also conducted for comparison purposes and literature data from the smooth-wall turbulent channel flow DNS of Hoyas & Jiménez (2006) at $Re_\tau = 2003$ were leveraged to support the conclusions made herein. While the rough-wall simulations are at relatively low Re_τ, they are the largest of their kind to date owing to the requirement to fully resolve the flow around the roughness to ensure that all dynamically significant scales of the flow were resolved while simultaneously capturing the largest scales of the flow that extend multiple *h* in the streamwise direction. Further, as reported by Bernardini & Pirozzoli (2011), AM effects begin to appear in smooth-wall flow at Re_τ as low as 400 (the same as the smooth-wall simulation presented herein) and roughness is now known to enhance the AM effect. We then leverage the AM effect to adapt the existing AM inner–outer model of Mathis *et al.* (2011) to predict the statistics of high-order moments of all three velocity components by introducing principal component analysis (PCA) to the model structure. Thus, as the present simulations provide the spatio-temporal data to investigate the effects of anisotropy in the universal signals obtained during the calibration of the AM model, the utility of this modelling framework can be extended to successfully predict the Reynolds shear stress, $\overline{u'v'}^+$, and statistics involving the spanwise velocity fluctuations, w'.

2. Numerical method

The governing equations solved herein are the incompressible Navier–Stokes equations, given by

$$\frac{\partial u_i}{\partial t} + u_j \frac{\partial u_i}{\partial x_j} = -\frac{\partial p}{\partial x_i} + \nu \frac{\partial^2 u_i}{\partial x_j \partial x_j} + f_i, \tag{2.1}$$

$$\frac{\partial u_i}{\partial x_i} = 0, \tag{2.2}$$

where x_i are the Cartesian coordinates and u_i are the velocity components. The notational convention adopted here is that u_1 (u), u_2 (v) and u_3 (w) denote the velocity components in the streamwise (x), wall-normal (y) and spanwise (z) directions, respectively, while p is the pressure (density assumed to be one) and ν is the kinematic viscosity. The forcing functions, f_i, ensure constant flow rate and the bulk Re is defined as $Re_b = U_b h/\nu$ based on the average streamwise velocity, U_b, and channel half-height, h.

The governing equations were solved with the open-source high-order spectral element method solver NEK5000, developed at Argonne National Laboratory (Fischer, Lottes & Kerkemeier 2014). The spectral element method is a high-order weighted-residual finite element method. The computational domain is discretized by partitioning it into E Nth-order hexahedral elements, where E is the number of spectral elements and N is the order of the tensor-product polynomials within each element. The physical space (x, y, z) is first transformed into the parametric space (r, s, t) where $-1 < r, s, t < 1$. Then, all numerical operations are performed in the parametric space; interpolation back to physical space is used for data storage and post-processing. Flow variables are represented by the tensor-product nodal basis as

$$u(x, y, z)|_{\Omega^e} = \sum_{i=0}^{N} \sum_{j=0}^{N} \sum_{k=0}^{N} u_{ijk}^e \psi_i(r) \psi_j(s) \psi_k(t), \tag{2.3}$$

where Ω^e is the computational domain for each element, ψ_i, ψ_j, ψ_k are the basis functions in the parametric space (r, s, t) and u_{ijk}^e are the nodal values of the flow quantity at points within the element. For the incompressible Navier–Stokes equations, the trial and test functions are chosen as the Legendre polynomials evaluated at the Gauss–Lobatto–Legendre (GLL) quadrature points. The non-uniform distribution of the GLL points enhances the stability of the numerical solver and allows point-wise quadrature operations to increase the efficiency of the method. Boundary conditions are enforced using the C^0 continuity properties of the interpolating functions (Fischer 2010). In these simulations, a polynomial order of $N = 7$ was used to maximize both spatial accuracy and computational efficiency for fast convergence of the simulations. The linear terms were treated implicitly with decoupling of the pressure and viscous terms while the nonlinear advection terms were treated explicitly using a third-order backward differencing scheme. The velocities were solved by three Helmholtz equations with efficient preconditioning techniques and the pressure was solved iteratively using a high-efficiency multigrid solver.

3. Simulation set-up

Direct numerical simulations of turbulent channel flow were performed with both walls roughened by a mat of hexagonally packed hemispheres as illustrated in
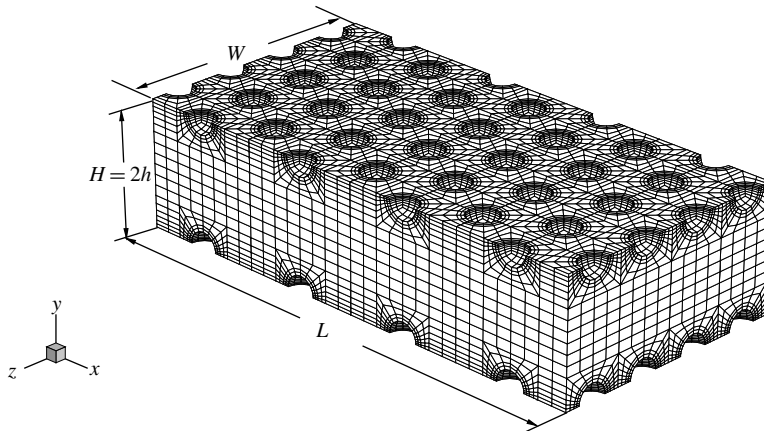
FIGURE 1. Prototypical computational mesh and domain size for the rough-wall simulations.

figure 1. The spectral element mesh is decomposed into two regions. Near the walls and surrounding the hemispheres (rough-wall region), dense body-fitted elements were employed to ensure that small turbulent scales were well-resolved around the roughness elements. Away from the walls, the majority of the domain (core region) was occupied by arrays of rectangular spectral element blocks aligned parallel to the homogeneous (x–z) plane whose wall-normal spacing was determined from previously published smooth-wall DNS at similar Re. No-slip boundary conditions were imposed on both walls and periodic boundary conditions were applied in both the streamwise and spanwise directions.

The domain size for all simulations was $L = 8\pi h$, $H = 2h$ and $W = 2\pi h$ in the streamwise, wall-normal and spanwise directions, respectively. Two-point correlations of the velocity fluctuations were found to decay approximately to zero within half of the domain (see appendix A), which ensured that the domain was large enough to contain the relevant turbulent structures, most importantly the large- and very-large-scale motions. These flow features can extend several channel half-heights in the streamwise direction in smooth-wall turbulent channel flow (Balakumar & Adrian 2007; Mathis *et al.* 2009*b*) and likely modulate the smaller scales in the near-wall region. This domain is about 25 times larger than the minimal computational box sufficient to sustain turbulence statistics as suggested by Jiménez & Moin (1991). Figure 2 shows actual configurations of hemispherical roughness, where the roughness height, k, is the radius of the hemisphere and d is the centre-to-centre spacing between hemispheres.

Table 1 summarizes the relevant flow and simulation parameters for each case. Three rough-wall simulations were performed at $Re_\tau = u_\tau h/\nu = 400$, where u_τ is the friction velocity defined by $u_\tau = \sqrt{\tau_w/\rho}$. The mean wall shear stress, τ_w, was calculated by averaging the total drag at the wall divided by the projected surface area of the wall. Note that the total drag at the wall was determined directly from the solver by integrating the pressure and viscous stresses over the surfaces in the flow direction. For these three rough-wall simulations, the roughness height was maintained as $k/h = 0.05$ while varying the pitch-to-height ratio between roughness elements in the range $d/k = 2$–4. Two additional rough-wall simulations were performed at $Re_\tau = 200$ and 600 to investigate Re effects for which the roughness heights were

Case	Re_b	Re_τ	k/h	d/k	L	H	W	Hemi. no.	Grid points	$\Delta x^+/\Delta z^+$	Δy^+_{min}
SM2000†	44 000	2003	—	—	$8\pi h$	$2h$	$3\pi h$	—	17 921 212 416	8.19/4.10	0.032
SM400	7043	400	—	—	$8\pi h$	$2h$	$2\pi h$	—	301 465 600	8.98/4.49	0.060
RH200-10-4	1864	200	0.100	4	$8\pi h$	$2h$	$2\pi h$	2304	679 477 248	4.98/2.81	0.088
RH400-20-4	4466	400	0.050	4	$8\pi h$	$2h$	$2\pi h$	9216	858 783 744	9.97/5.61	0.154
RH400-20-3	4568	400	0.050	3	$8\pi h$	$2h$	$2\pi h$	16 000	1 245 184 000	7.18/4.48	0.102
RH400-20-2	5742	400	0.050	2	$8\pi h$	$2h$	$2\pi h$	33 120	1 420 656 640	7.80/4.48	0.107
RH600-30-4	8346	600	0.034	4	$8\pi h$	$2h$	$2\pi h$	21 504	1 431 306 240	9.62/5.61	0.231

TABLE 1. Relevant flow and simulation parameters for each case. The roughness height, k, is the radius of hemispheres; d is the centre-to-centre spacing between hemispheres. h is the channel half-height; $Re_b = U_b h/\nu$ is the bulk Re; $Re_\tau = u_\tau h/\nu$ is the friction Re; the inner-scaled roughness height, $k^+ = u_\tau k/\nu = 20$, is fixed for all rough-wall cases. SM2000† is reported by Hoyas & Jiménez (2006) and was retrieved from http://turbulence.ices.utexas.edu.
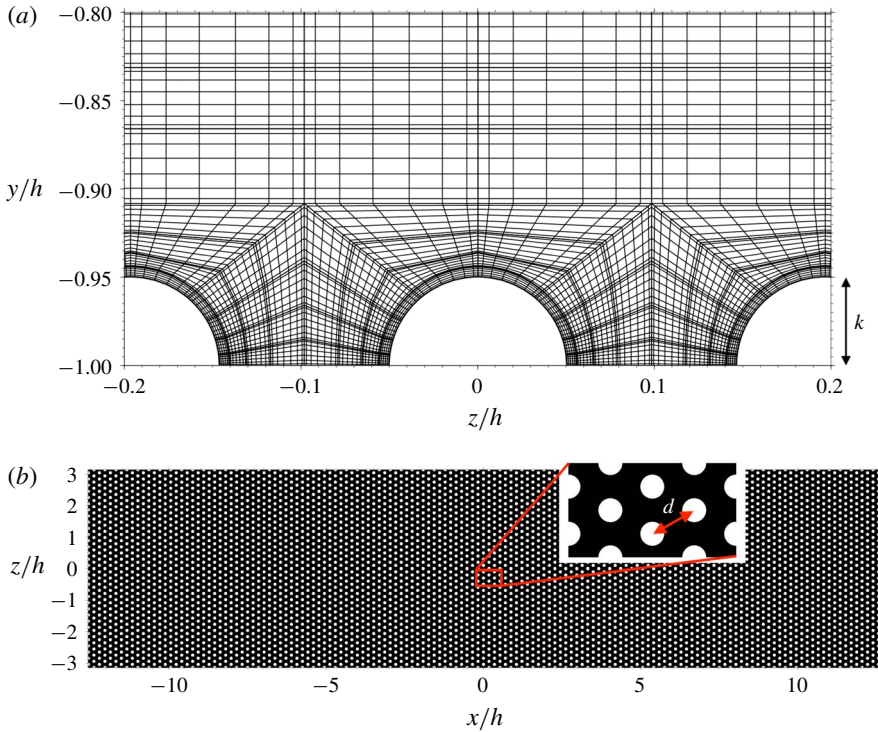
FIGURE 2. (Colour online) Configurations of the hemispherical roughness. (*a*) Mesh distribution around the hemispherical roughness. (*b*) Hexagonal packing of roughness elements for simulation RH400-20-4.

$k/h = 0.1$ and $k/h = 0.034$, respectively, the element spacing was $d/k = 4$. All rough-wall simulations utilized $k^+ = 20$. In addition, table 1 summarizes parameters for a smooth-wall channel flow simulation conducted at $Re_\tau = 400$ and smooth-wall DNS data at $Re_\tau = 2003$ reported by Hoyas & Jiménez (2006). Both smooth-wall cases served as baselines against which the rough-wall cases are compared.

In table 1, Δx^+ and Δz^+ denote the average streamwise and spanwise grid spacings, respectively, in inner units. The domain in the wall-normal direction was discretized non-uniformly such that the corner points of each spectral element were distributed based on the Chebyshev collocation points given by

$$y_j = (N+1)\frac{\cos(j-1)}{n_y - 1}, \tag{3.1}$$

where y_j is the location of the corner point of the jth spectral element in the wall-normal direction, N is the polynomial order of the tensor product and n_y is the total number of elements in the wall-normal direction. For all rough-wall cases, the wall-normal origin was positioned at the base plane of the hemispheres of both walls. Further, Δy_{min}^+ denotes the first collocation point above the wall in inner units. The meshes around the roughness elements in all cases were developed based on a mesh scheme described in appendix B. By refining this mesh scheme in the streamwise, wall-normal and spanwise directions and comparing the Reynolds stresses obtained from these meshes, the statistics produced by this mesh scheme were in good
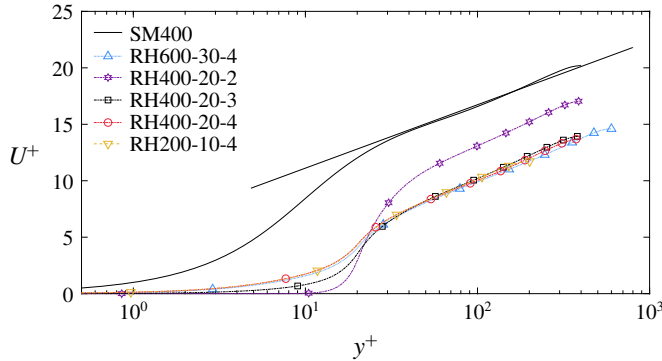
FIGURE 3. (Colour online) Mean streamwise velocity profiles for smooth- and rough-wall cases at various Re. Straight line reflects the log law: $U^+(y^+) = (1/0.41) \ln(y^+) + 5.5$.

agreement with those using refined meshes. Thus, the current meshes are appropriate for the goals of this study and ensure that flow within the roughness sublayer was well resolved. Finally, smooth- and rough-wall simulations are denoted by SM and RH, respectively.

All simulations were carried out at Department of Defense High Performance Computing Centers on massively parallel platforms using the MPI2.0 standards. The statistics for the mean velocities, velocity gradients and Reynolds stresses were collected after initial transients for approximately ten flow-through times to ensure converged statistics, which is consistent with previous studies of turbulent channel flow (Jiménez & Hoyas 2008, for example).

4. Flow statistics

4.1. *Mean velocity profiles*

Mean velocity profiles are obtained for each case by averaging the streamwise velocity field in the wall-parallel plane at each wall-normal location. Figure 3 shows the inner-scaled, mean streamwise velocity, U^+, for all cases, including that of the smooth-wall DNS at $Re_\tau = 400$. The log law $U^+(y^+) = (1/0.41) \ln(y^+) + 5.5$ is also included. While viscous stress is the only contributor to the drag in the smooth-wall case, figure 5 highlights the increased drag produced by roughness, including form-drag contributions to the overall wall shear stress. This increased drag modifies the mean velocity profile by an approximately constant downward shift in the log region of the flow, ΔU^+. This downward shift is observed for all rough-wall cases and can be determined by fitting the rough-wall mean velocity profiles with the log law as

$$U^+(y^+) = \frac{1}{\kappa} \ln(y^+) + 5.5 - \Delta U^+. \tag{4.1}$$

The effective wall-normal origin, d_0^+, is also determined by fitting the slope of the log law assuming $\kappa = 0.41$. Table 2 summarizes these roughness-induced parameters for all cases. Finally, the equivalent sand-grain roughness height, k_s^+, for each case can be determined by matching the ΔU^+ observed to the sand-grain size that yields an equivalent ΔU^+ from the measurements of Nikuradse (1933). The main observation in figure 3 is the clustering of profiles based on the degree of packing of the surface

Case	d_0^+	ΔU^+	k_s^+	C_f	Type
SM400	—	—	—	0.0065	—
RH200-10-4	5.6	6.6	51	0.0232	k-type
RH400-20-4	5.8	6.6	51	0.0160	k-type
RH400-20-3	10.3	6.2	43	0.0153	k-type
RH400-20-2	15.2	3.2	8	0.0097	d-type
RH600-30-4	6.0	6.6	51	0.0137	k-type

TABLE 2. Summary of the roughness-induced flow parameters: d_0^+ is the effective wall-normal origin, ΔU^+ is the roughness function, k_s^+ is the inner-scaled equivalent sand-grain roughness height and $C_f = 2(u_\tau/U_b)^2$ is the skin-friction coefficient.

roughness. The closely packed (hemispheres touching) case RH400-20-2 has a mean velocity that is intermediate to the smooth-wall cases and all other rough-wall cases. When the packing density of the roughness elements is high (i.e. low d), they effectively shelter one another and form narrow recirculation regions that isolate the outer flow from the roughness sublayer (Jiménez 2004). Thus, the densely packed roughness in the RH400-20-2 cases is classified as the 'd-type' roughness whereas the cases RH400-20-3 and RH400-20-4 are commonly referred to as the 'k-type' roughness, based on the classification first introduced by Perry *et al.* (1969). Moreover, the mean velocity profiles for the rough-wall cases at $Re_\tau = 200$ (RH200-10-4) and 600 (RH600-30-4) collapse very well in the log layer with RH400-20-4. This collapse is consistent with previous studies (Nikuradse 1933; Colebrook & White 1937; Perry *et al.* 1969, among others) wherein for 'k-type' roughness, the primary factor in determining ΔU^+ is k^+ compared to other geometrical parameters. For 'k-type' roughness, ΔU^+ can be related to k_s^+ via the study of Nikuradse (1933) through the fully rough asymptote given by

$$\Delta U^+ = \frac{1}{\kappa}\ln(k_s^+) + A - 8.5. \qquad (4.2)$$

Flows are commonly considered as fully rough for $k_s^+ \gtrsim 70$ for which the form drag dominates over viscous contributions. In the present study, the equivalent roughness heights $k_s^+ < 70$, indicating that our rough-wall flows are still in the transitionally rough regime. For 'd-type' roughness, however, k_s is determined by the half-channel height as $k_s \approx 0.02h$ (Jiménez 2004).

The drag enhancement by roughness can be quantified by the skin-friction coefficients $C_f \equiv 2(u_\tau/U_b)^2$ (see table 2). Compared to the smooth-wall case, the rough-wall skin-friction coefficients are larger for all cases. In addition, as the pitch-to-height ratio of the roughness elements is increased, the skin-friction coefficient increases from 0.0097 for RH400-20-2 to 0.016 for RH400-20-4. This observation is expected since increasing the pitch-to-height value promotes momentum transfer within the roughness sublayer and enhances the pressure difference across the roughness elements (Bailon-Cuba, Leonardi & Castillo 2009). It is also noted that the difference is small between $d/k = 3$ and 4, as it has been reported that the effect of roughness packing density saturates near $d \approx 3$–$4k$ (Jiménez 2004).

4.2. *Reynolds stresses*

Figure 4 presents components of the Reynolds stress tensor in inner units for the smooth- and rough-wall cases. As shown in figure 4(*a*), the peak streamwise normal
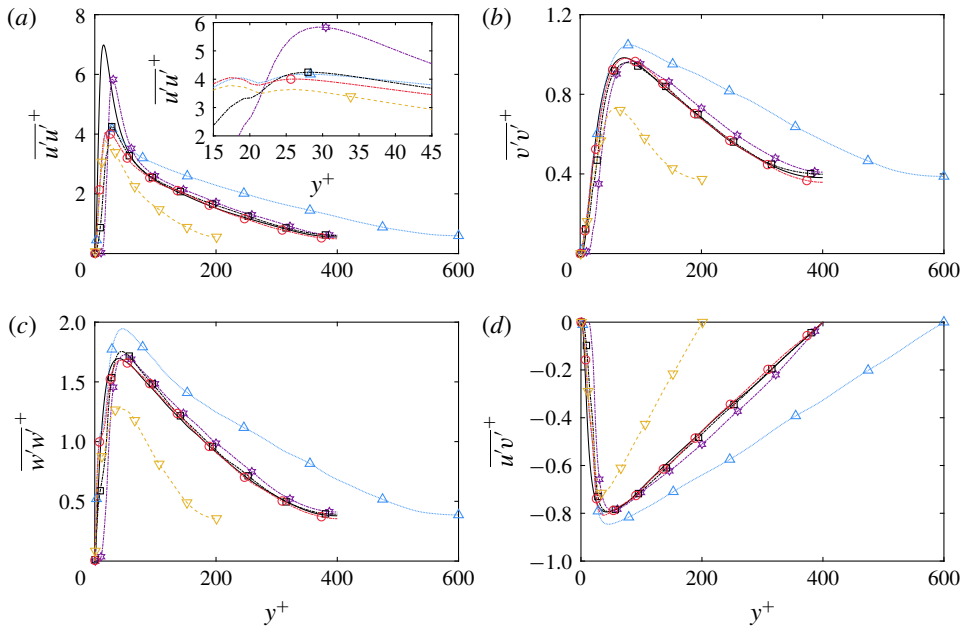
FIGURE 4. (Colour online) Reynolds stress components versus y^+ for the smooth- and rough-wall cases. The inset of (*a*) shows $\overline{u'u'}^+$ near the roughness crests ($y^+ = 20$) for all rough-wall cases. Legend as in figure 3.

stress, $\overline{u'u'}^+$, is reduced significantly for flows over rough surfaces. A large reduction is observed for RH400-20-4 and similarly for RH400-20-3 owing to the break-up of vortical structures in the streamwise direction. However, the reduction of peak $\overline{u'u'}^+$ is less significant in the case RH400-20-2, likely due to the sheltering effect of closely packed roughness elements, which renders this case more hydrodynamically similar to smooth-wall flow. In addition, the location of peak $\overline{u'u'}^+$ tends to shift farther away from the wall as the roughness elements become more compacted. Moreover, $\overline{u'u'}^+$ exhibits an inner peak below the roughness crest $y^+ = 20$ as shown in the inset of figure 4(*a*) for the cases RH200-10-4, RH400-20-4 and RH600-30-4 with the same k^+ and packing density. The formation of this inner peak is likely due to the vortical structures formed in the cavity between roughness elements which promote the streamwise velocity fluctuations below the roughness crest. This effect is weakened in the cases RH400-20-3 and RH400-20-2 with closely spaced roughness since the strength of the vortical structures declines as the roughness elements move closer to each other and the blocking effect of the hexagonal packing pattern becomes relevant for higher packing densities. This trend eventually leads to the destruction of the inner peak in $\overline{u'u'}^+$. Above the roughness crest, the profiles develop an outer peak near $y^+ \approx 25$–30 for the rough-wall cases, owing to stronger production of turbulence induced by the wakes of the roughness elements. Figures 4(*b*), 4(*c*) and 4(*d*) show the wall-normal, $\overline{v'v'}^+$, the spanwise, $\overline{w'w'}^+$, and the shear stress, $\overline{u'v'}^+$, respectively. When compared to smooth-wall flow, these turbulent stresses are less sensitive to the roughness. The sheltering effect is still apparent as the profiles tend to shift slightly towards the outer layer with increasing packing density. The shear stress, $\overline{u'v'}^+$, falls quickly onto a straight line for $y^+ > 80$, as expected for fully developed
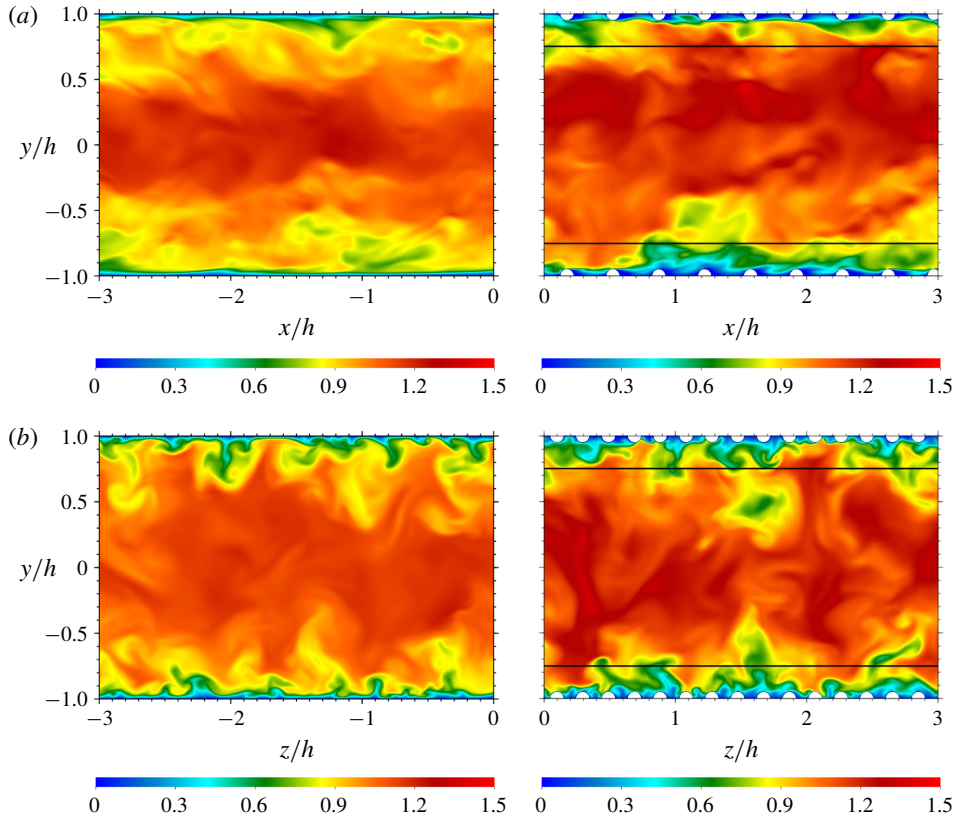
FIGURE 5. (Colour online) Representative visualizations of the instantaneous streamwise velocity, u, normalized by the average streamwise velocity U_b, in the (*a*) x–y plane and (*b*) y–z plane for the smooth-wall case SM400 (left) and the rough-wall case RH400-20-4 (right). Lines in the rough-wall cases (right) demarcate $5k$ away from the top and bottom walls as a qualitative measure of the roughness sublayer.

turbulent channel flow. For a given roughness height and spacing, increasing *Re* tends to enhance the intensity of all Reynolds stresses and shift their peaks towards the wall.

5. Spatial structure of the flows

Figure 5 shows representative visualizations of the instantaneous streamwise velocity u, normalized by the average streamwise velocity U_b, in the x–y and y–z planes for the rough-wall case RH400-20-4 (right) in comparison with the smooth-wall case SM400 (left). Intense turbulent motions are readily apparent near the wall in both cases; however, the hemispherical roughness induces flow separation just downstream of each element, which yields form-drag contributions to the overall drag. In addition, roughness enhances the turbulence levels in a certain region above the roughness crest into the log region. The horizontal lines in the rough-wall cases delineate a $5k$ distance from each rough wall as a qualitative measure of the depth of the roughness sublayer (i.e. the region near the wall where roughness directly impacts the flow). The most intense turbulent fluctuations are primarily contained within this roughness
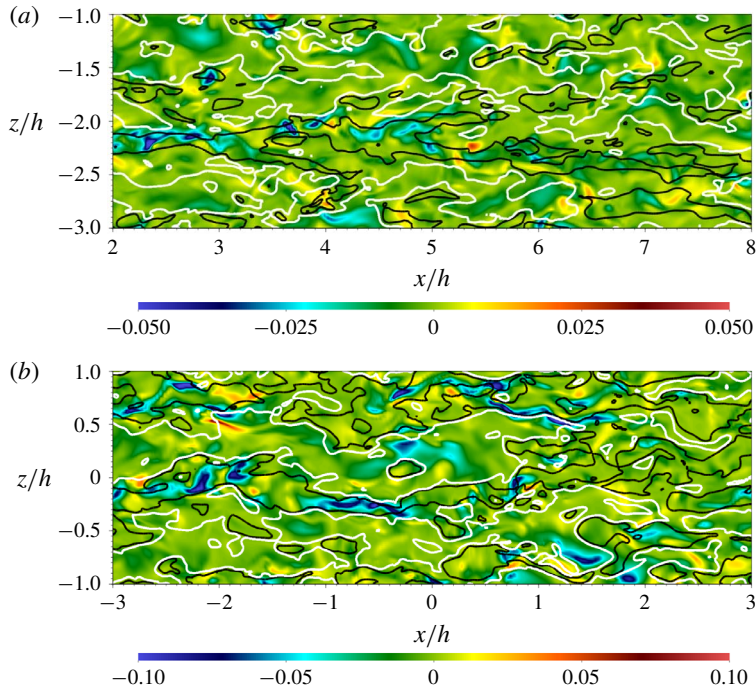
FIGURE 6. (Colour online) Representative visualizations of the instantaneous Reynolds-shear-stress contributions, $u'v'$, for the (*a*) smooth-wall case SM400 and the (*b*) rough-wall case RH400-20-4 at $y^+ = 100$ (corresponds to $y = 5k$ for the rough-wall case). Line iso-contours: LMRs (black, $u/U_m < 0.9$) and HMRs (white, $u/U_m > 1.1$) from the $y^+ = 50$ plane.

sublayer in both planes visualized. Quadrant analysis has previously shown that this effect is strongly correlated to the vigorous ejections of low streamwise momentum fluid away from the wall and sweeps of high streamwise momentum fluids towards the wall. Coceal *et al.* (2007) showed that these events are not randomly distributed in the flow but well organized in certain regions spanning a range of scales. Importantly, the trains of vortices shed from the hemispherical roughness elements induce greater ejections/sweeps of fluid away/towards the wall which strongly contributes to the mean Reynolds shear stress.

Figures 6–8 present representative visualizations of the instantaneous Reynolds-shear-stress contributions, $u'v'$, for the smooth- (top) and rough-wall (bottom) cases in the wall-parallel x–z plane at three wall-normal locations at the same instant in time. It is well established that both smooth- and rough-wall flows embody streamwise-elongated regions of low ($u' < 0$) and high ($u' > 0$) streamwise momentum that alternate in the spanwise direction (Ganapathisubramani, Longmire & Marusic 2003; Tomkins & Adrian 2003; Ganapathisubramani *et al.* 2005; Wu & Christensen 2010, for example), whose streamwise extent can exceed multiple outer length scales (*h*, for channel flow) and are thus termed very-large-scale motions (Kim & Adrian 1999) or superstructures (Hutchins & Marusic 2007*b*). The imprints of low momentum regions (LMRs) and high momentum regions (HMRs) extend from the outer layer through to the near-wall region (Hutchins & Marusic 2007*a*) and are believed to drive the modulation of the small-scale, near-wall motions (Mathis, Hutchins & Marusic
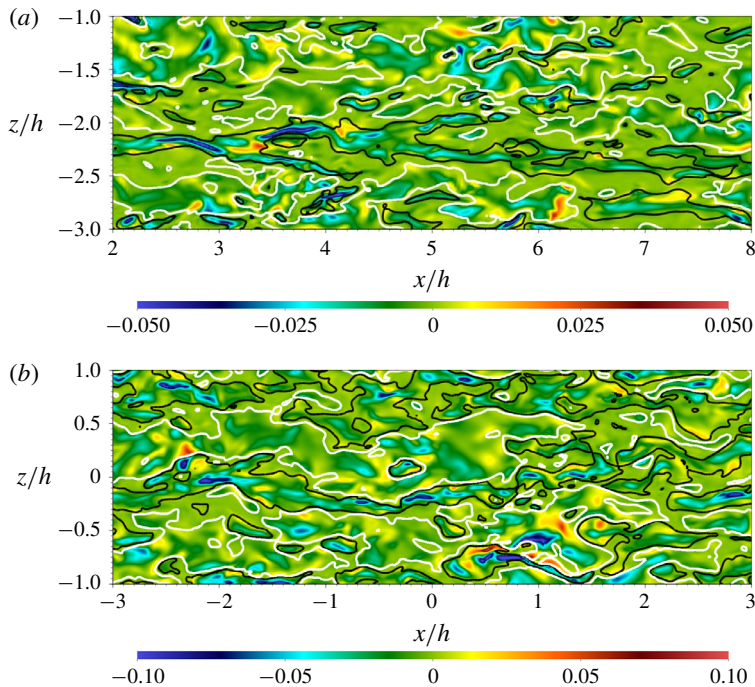
FIGURE 7. (Colour online) As in figure 6, but at $y^+ = 50$ (corresponds to $y = 2.5k$ for the rough-wall case).

2009*a*). In addition, they contribute heavily to the Reynolds shear stress, with LMRs producing intense ejections of low streamwise momentum fluid away from the wall and the HMRs generating intense sweeps of high streamwise momentum towards the wall. Further, previous studies have found that LMRs represent the *x*–*z* signature of large-scale hairpin vortex packets which are known to occur in both smooth- and rough-wall flows (Christensen & Adrian 2001; Ganapathisubramani *et al.* 2003; Adrian 2007; Volino *et al.* 2007; Wu & Christensen 2010, for example). Finally, it should be noted that these elongated LMRs and HMRs are entirely distinct from the low-speed streaks that occur within the buffer layer of wall turbulence.

With this background in mind, figures 6–8 embody very similar features of LMRs and HMRs in the $y^+ = 100$, 50 and 25 wall-parallel planes, respectively, which corresponds to $y = 5k$, $2.5k$ and $1.25k$ for the rough-wall cases, respectively (again, the three wall-parallel planes for the smooth case were taken at the same instant in time, as were the three for the rough-wall case). Line iso-contours of instantaneous low momentum regions (LMRs; $u/U_m < 0.9$) and high momentum regions (HMRs; $u/U_m > 1.1$) are also included from the $y^+ = 50$ plane to illustrate the imprints of the outer larger-scale motions on the flow within and below the log layer (Here, U_m is the local mean streamwise velocity). These iso-contours bound the spanwise extent of streamwise-elongated LMRs and HMRs that alternate in the spanwise direction in both the smooth- and rough-wall flows, within which intense negative contributions to $u'v'$ are noted (ejections in LMRs and sweeps in HMRs). Beginning with the $y^+ = 100$ fields ($y = 5k$ for the rough-wall case, which corresponds to the outer edge of the roughness sublayer) in figure 6, an approximately 6h-long LMR (black lines) is apparent near $z = -2.2h$ in the instantaneous smooth-wall field that is bounded on
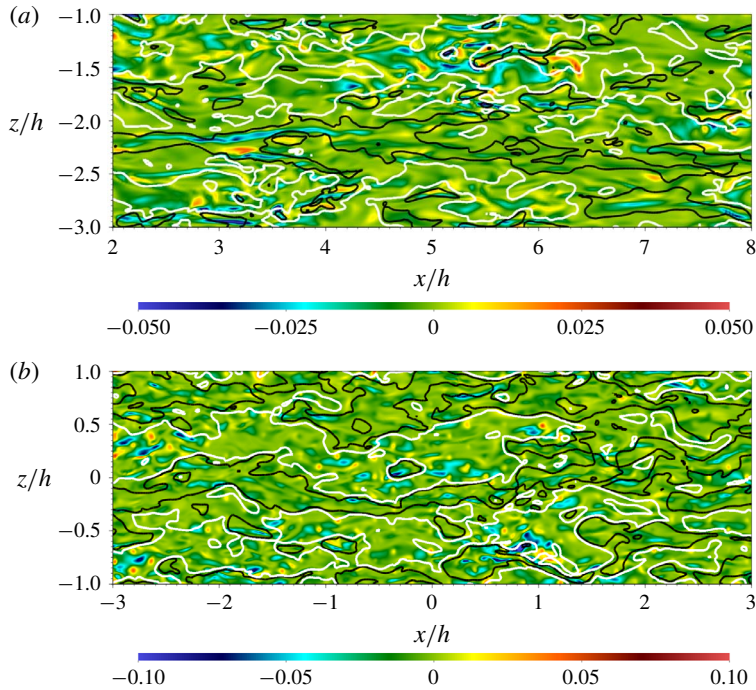
FIGURE 8. (Colour online) As in figure 6, but at $y^+ = 25$ (corresponds to $y = 1.25k$ for the rough-wall case).

both sides by elongated HMRs (white lines) and within which intense $u'v'$ events are apparent. Similar features are readily apparent in the instantaneous rough-wall field, where a 5–6h-long LMR (black lines) is noted at roughly $z = 0$ in this field that is also bounded on both sides by elongated HMRs and within which strong negative $u'v'$ contributions are noted, although the intensity of these events is more than that of the smooth-wall case. These features are entirely consistent with previous studies at similar and higher Re and the striking consistency between these outer-layer spatial features at $y^+ = 100$ of the smooth- and rough-wall flows is consistent with the notion of outer-layer similarity where the underlying spatial structure is similar even in the presence of roughness (Raupach *et al.* 1991; Flack *et al.* 2005; Wu & Christensen 2007, among others).

Similar LMR and HMR signatures are readily apparent in figure 7 at $y^+ = 50$ and figure 8 at $y^+ = 25$. In particular, one can identify intense $u'v'$ events at $y^+ = 100$ and find their signatures still apparent at these lower wall-normal locations at similar spatial locations as they were sampled, indicating that these LMRs and HMRs and their associated $u'v'$ contributions occupy this wall-normal extent, $y^+ = 25$–100 and that roughness enhances the intensity of these events compared to smooth-wall flow. These observations are again consistent with previous ones in smooth- and rough-wall flow, which are interpreted as the imprint of the LMRs and HMRs in the near-wall region and represents a distinct linkage between these regions of the flow. Thus, consistency in these structural attributes between smooth- and rough-wall flow, particularly the imprint of outer-layer motions in the near-wall region, explains why AM effects have been identified in rough-wall turbulence (Anderson 2016;

Squire *et al.* 2016; Pathikonda & Christensen 2017*a*) and set the foundation for the physics-based modelling proposed herein.

6. More advanced statistical tools

6.1. *Amplitude modulation of spatial signals*

As mentioned previously, experimental measurements in smooth-wall turbulent boundary layers (Marusic *et al.* 2010; Mathis *et al.* 2011) at high *Re* revealed that the large-scale motions in the outer region amplitude modulate the small-scale motions in the near-wall region, with this modulation increasing in strength with *Re*. Such effects were initially demonstrated by decoupling temporal signals of the point-wise measured fluctuating streamwise velocity into large- and small-scale components with an appropriate streamwise filter scale (converted to time with Taylor's hypothesis) that resided between these two scales. By analysing the correlation between the large-scale signal and the filtered envelope of the small-scale signal determined with the Hilbert transform, Mathis *et al.* (2009*a*), Marusic *et al.* (2010) have shown that the near-wall small-scale turbulence is strongly modulated by the outer-layer large-scale motions.

The scale decomposition procedure for the fluctuating streamwise velocity signal was originally outlined by Mathis *et al.* (2009*a*). Long records of fluctuating streamwise velocity were sampled at a sufficient rate to ensure that the small and large scales of the flow were simultaneously captured. These fluctuating velocity signals were originally time series and reinterpreted as spatial signals using Taylor's hypothesis (i.e. $\kappa_x = 2\pi f/U$). In the current DNS of turbulent channel flow, it is more convenient and less expensive to sample data over the entire spatial domain (i.e. entire wall-parallel planes) at instants in time and average in the spanwise direction to ensure convergence of statistics. Therefore, all velocity signals in the current work were sampled in space rather than time. This sampling was accomplished by interpolating the velocity from the nodal points of the finite elements onto a uniform grid at multiple wall-parallel planes.

Similar to the AM analysis framework reported by Mathis *et al.* (2009*a*), the fluctuating velocity signals $u'^+(x)$ herein were decomposed spatially in the streamwise direction using a sharp spectral filter as

$$u'^+(x) = u_L'^+(x) + u_S'^+(x), \tag{6.1}$$

where the filter operation is applied to obtain the large-scale component

$$u_L'^+(x) = \int_D G(r)u'^+(x - r)\,\mathrm{d}r, \tag{6.2}$$

with the kernel of the sharp spectral filter given by

$$G(x) = \frac{\sin(2\pi x/h)}{\pi x}. \tag{6.3}$$

The cutoff wavenumber corresponds to the cutoff wavelength, λ_c, through

$$\kappa_c = \frac{2\pi}{\lambda_c} = \frac{2\pi}{h}, \tag{6.4}$$

which is equivalent to the cutoff angular frequency ω_c used to decompose a temporal signal by

$$\kappa_c = \frac{2\pi}{h} = \frac{2\pi/U(y)}{h/U(y)} = \frac{2\pi/t_o}{U(y)} = \frac{\omega_c}{U(y)}. \tag{6.5}$$

Case	NX	NY	NZ	δx^+	δz^+	y_O^+
SM2000	4096	1024	3072	12.3	6.13	198.2
SM400	1280	385	640	7.85	3.93	101.4
RH200-10-4	1152	129	512	4.36	2.45	81.2
RH400-20-4	1280	385	640	7.85	3.93	101.4
RH400-20-3	1280	385	640	7.85	3.93	101.4
RH400-20-2	1280	385	640	7.85	3.93	101.4
RH600-30-4	1600	449	800	9.42	4.71	125.7

TABLE 3. Parameters of the sampled planes. NY is the number of planes in the wall-normal direction; NX–NZ are the number of sampling points in each plane in the streamwise and spanwise directions, respectively; δx^+–δz^+ are the corresponding uniform sampling spacings; y_O^+ is the outer-layer wall-normal reference location.

Here, $t_0 = h/U(y)$ is the eddy turnover time at any specific wall-normal location based on the local mean velocity, $U(y)$. The sharp spectral filter eliminates the Fourier modes of any wavenumber $|\kappa_x|$ greater than the cutoff wavenumber κ_c with no effect on the lower modes.

The details of the sampled planes for all cases are summarized in table 3. The spacing between sampled points in each plane was constant as indicated by δx^+ and δz^+ along the streamwise and spanwise directions, respectively. These spacings were chosen to be comparable to the grid spacings to ensure that the small-scale features were captured and the energy in the largest scales was converged with sufficient samples.

At a given wall-normal location, the streamwise velocity signals are decomposed in the x-direction at every z-coordinate. An example of this spatial scale decomposition in the near-wall region for the smooth-wall flow at $Re_\tau = 400$ is shown in figure 9. Consistent with the experimental observations (Mathis *et al.* 2009*a*), the large-scale signal captures the general trend of the raw fluctuating signal, with the occurrence of the negative large-scale signal tends to amplitude modulate the small-scale signal. This can be seen, for example, in the region of the dashed vertical lines in figure 9(*c*). In contrast, the small-scale signal embodies more intermittent and intense velocity fluctuations associated with small-scale features of the flow.

To quantify the effects of amplitude modulation, the Hilbert transform is employed to extract the envelope of the small-scale signal as

$$E\{u_S'^+\}(x) = \sqrt{u_S'^{+2}(x) + \mathcal{H}\{u_S'^+\}^2(x)}, \qquad (6.6)$$

where the Hilbert transform is given by

$$\mathcal{H}\{u_S'^+\}(x) = \frac{1}{\pi} P \int_{-\infty}^{\infty} \frac{u_S'^+(r)}{x - r} \, dr. \qquad (6.7)$$

Here, P is the Cauchy principal value of the integral and r is the spatial shift in the streamwise direction. Owing to the multi-scale nature of turbulence, the envelope returned by the Hilbert transform generally contains not only the large-scale modulation effects but also the small-scale variations carried by the original signal.
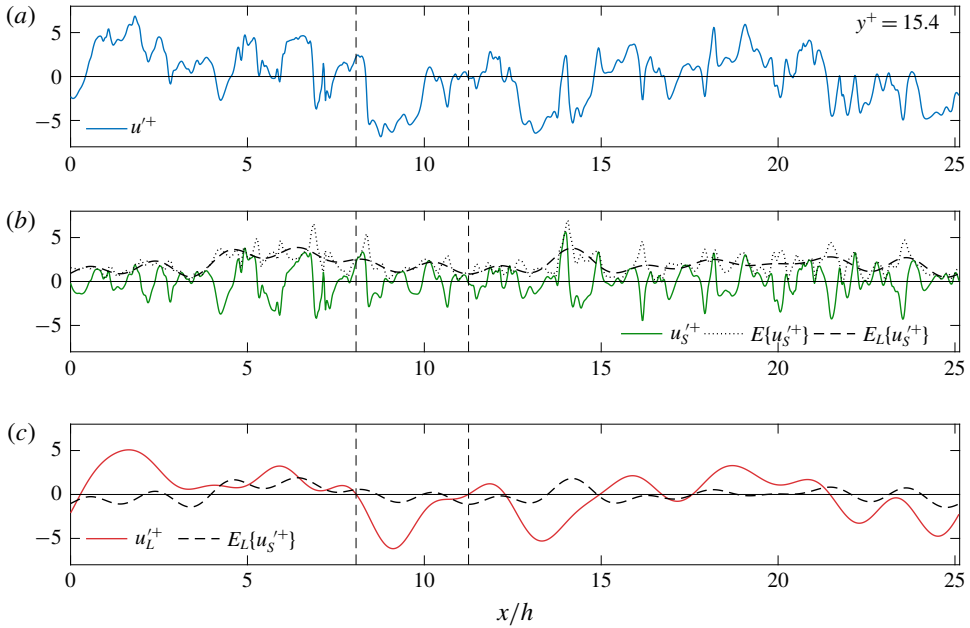
FIGURE 9. (Colour online) Spatial velocity decomposition and comparison with the envelopes at $y^+ = 15.4$ for the smooth-wall case at $Re_\tau = 400$. Vertical lines denote regions of negative excursion of the large-scale signal. (*a*) Raw streamwise velocity signal. (*b*) Small-scale signal, envelope and filtered envelope. (*c*) Large-scale signal and filtered envelope (mean removed).

Therefore, this envelope is filtered at the same cutoff wavenumber as the large-scale signal

$$E_L\{u_S'^+\}(x) = \int_D G(r)E\{u_S'^+\}(r-x)\,\mathrm{d}r, \qquad (6.8)$$

which thus returns the large-scale envelope of the small-scale signal, $E_L\{u_S'^+\}(x)$. Figure 9(*b*) illustrates an example of the envelope of the small-scale signal and the resulting filtered envelope for the smooth-wall case at $Re_\tau = 400$. It is readily seen that the filtered envelope closely resembles the large-scale signal as shown in figure 9(*c*).

Adopting the approach of Mathis *et al.* (2009*a*), the amplitude modulation of a fluctuating velocity signal, u'^+, is formally defined as the correlation coefficient between the large-scale envelope of the small-scale signal, $E_L\{u_S'^+\}$, and the large-scale signal, $u_L'^+$, at any two wall-normal positions y_1^+ and y_2^+ as

$$AM\{u'^+\} = R_u(y_1^+; y_2^+) = \frac{\overline{E_L\{u_S'^+\}(y_1^+)\,u_L'^+(y_2^+)}}{\sqrt{\overline{E_L\{u_S'^+\}(y_1^+)^2}}\sqrt{\overline{u_L'^+(y_2^+)^2}}}. \qquad (6.9)$$

Note that each term of this correlation coefficient is first calculated individually at every z-coordinate and then averaged across the z-direction. While the framework of amplitude modulation has been predominantly applied to just the streamwise velocity component, its use is extended to all three velocity components in the smooth- and

rough-wall flows studied herein. Following the definition given in Talluru *et al.* (2014), the AM correlation coefficients for v' and w' are defined by

$$AM\{v'^{+}\} = R_v(y_1^+; y_2^+) = \frac{\overline{E_L\{v_S'^+\}(y_1^+) \; u_L'^+(y_2^+)}}{\sqrt{\overline{E_L\{v_S'^+\}(y_1^+)^2}}\sqrt{\overline{u_L'^+(y_2^+)^2}}}, \tag{6.10}$$

and

$$AM\{w'^{+}\} = R_w(y_1^+; y_2^+) = \frac{\overline{E_L\{w_S'^+\}(y_1^+) \; u_L'^+(y_2^+)}}{\sqrt{\overline{E_L\{w_S'^+\}(y_1^+)^2}}\sqrt{\overline{u_L'^+(y_2^+)^2}}}. \tag{6.11}$$

Figure 10 demonstrates the AM correlation coefficients in the wall-normal direction for all velocity components extracted from the DNS of turbulent channel flows over various rough surfaces (refer to table 1 for case labels). Here, the large-scale signal is taken as that embodied in u' regardless of the velocity component considered, consistent with Talluru *et al.* (2014), as v' and w' primary reflect signatures of smaller and intermediate scales of the flow while u' embodies larger-scale ones (Jiménez & Hoyas 2008).

In the aforementioned experimental studies, AM effects were investigated using single-point measurements, so the AM correlation coefficient was defined by setting $y_1^+ = y_2^+$ in (6.9). In this regard, the large scales were correlated with the filtered envelope of the small scales at the same wall-normal location. Equivalent single-point AM correlation coefficients were calculated for the DNS cases herein are shown in figure 10(*a*,*c*,*e*) for u', v' and w', respectively. For the streamwise velocity component, R_u, the correlation coefficient shows a strong AM effect near the wall in the smooth-wall cases (the current $Re_\tau = 400$ DNS and the $Re_\tau = 2003$ from Hoyas & Jiménez (2006)). This is particularly evident for the higher-Re smooth-wall case which is quite consistent with the results reported by Mathis *et al.* (2009*a*) for $Re_\tau = 2800$ as reproduced in figure 10(*a*). However, in contrast to previous boundary-layer observations, the absence of high negative correlation beyond the log region is observed in the smooth-wall channel cases. Mathis *et al.* (2009*a*) attributed this strong negative correlation in turbulent boundary layers to intermittency in the wake region. As the present channel flows are fully developed, no such wake region exists near the centreline and thus this negative correlation region is not noted herein and the correlation instead exhibits a relatively flat shape in the log region. This observation agrees with the results reported by Mathis *et al.* (2009*b*) wherein they compared AM effects in turbulent boundary-layer, pipe and channel flows and showed that such behaviour in the outer region is dependent on the flow geometry. Similar trends are observed herein for the AM correlation coefficients for the wall-normal, R_v, and spanwise, R_w, velocity components as shown in figures 10(*c*) and 10(*e*), respectively. Thus, the large-scale signature amplitude modulates the small-scale velocity fluctuations across all three velocity components, consistent with experimental results reported by Talluru *et al.* (2014) in a turbulent boundary layer and recent DNS work in a minimal channel reported by Yin, Huang & Xu (2018).

The effects of roughness are clear in the single-point AM correlations presented in figure 10(*a*,*c*,*e*). For all velocity components, the presence of roughness enhances the degree of AM in the immediate region above the roughness, but still deep in the roughness sublayer, compared to smooth-wall flow at the same Re_τ, implying that localized small-scale structures in the near-wall region of rough-wall flow experience enhanced modulation by the large-scale structures. With regard to element spacing,
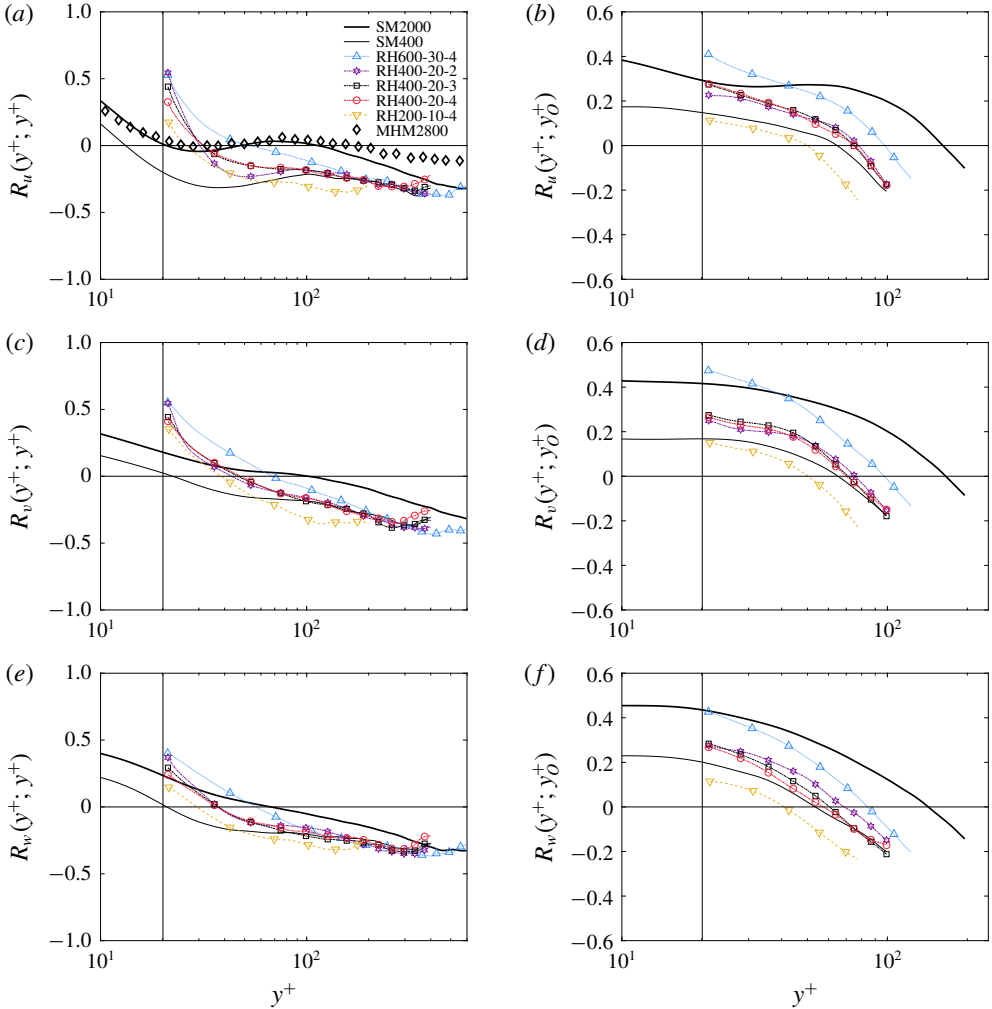
FIGURE 10. (Colour online) Amplitude modulation correlation coefficients for the smooth-
and rough-wall cases. (a,c,e) Single-point AM; (b,d,f) two-point AM (y_O^+ for each case is
listed in table 3). The single-point AM in smooth-wall flow at $Re_\tau = 2800$ from Mathis
et al. (2009a) is also included for comparison and is labelled as MHM2800. Vertical line
denotes the location of the roughness crest $k^+ = 20$.

the degree of modulation is approximately the same for most wall-normal positions,
except very close to the roughness crest where the greatest enhancement is found in
the case with the closest-packed hemispheres. This localized effect diminishes as the
element spacing increases. Further, the single-point AM correlations collapse very well
in the outer-layer region between the smooth- and rough-wall cases at fixed $Re_\tau = 400$,
further evidence of outer-layer similarity for these surface conditions. This outer-layer
similarity of AM effects between the smooth and rough cases suggests that roughness
alters the flow up to approximately $y^+ = 100$, or $5k$ from the wall. This latter measure
of the roughness-sublayer thickness is in agreement with previous observations for 3-D
roughness (Flack, Schultz & Connelly 2007; Wu & Christensen 2007). Interestingly,
for the rough cases, the zero crossings of R_u, R_v and R_w occur below the log region,

in contrast to that of the SM2000 high-*Re* case presented, where the zero crossings for all three correlations occur at approximately the same wall-normal location ($y^+ \approx$ 100) in the log region. This behaviour is expected since the large-scale structures become progressively energetic and have stronger modulation effects as *Re* increases. Nevertheless, the wall-normal trends of the DNS cases presented herein share very similar overall characteristics to this higher-*Re* smooth-wall case.

Though these single-point AM correlation coefficients provide a reasonable estimate of the degree of AM of the outer large scales on the small scales (Mathis *et al.* 2009*a*), this approach presumes that the large-scale signal at the single-point wall-normal location is fully reflective of the true large-scale signature in the outer region. While studies of smooth-wall flow show this assumption to be valid when comparisons are made between single- and two-point AM correlations, roughness directly perturbs the flow near the wall, which could include perturbation of the large scales as well. Thus, additional insight about the interactions between the inner, small-scale and outer, large-scale turbulence can be gained by computing the synchronized two-point AM correlation coefficients, where the large-scale signal is taken directly from the outer layer. Doing so directly demonstrates how near-wall turbulence is modulated by the larger-scale motions in the outer layer in an nonlinear manner that is free of cross-contamination that may occur in the single-point AM approach. As shown in figure 10(*b*,*d*,*f*), the two-point AM correlation coefficients show consistent *Re* trends for all velocity components and surface conditions. It is more evident that the AM effect is enhanced by roughness and this measure of AM effects is less sensitive to the element spacing. Furthermore, the presence of AM in the $Re_\tau = 400$ smooth-wall case as well as all roughness cases is consistent with the work by Bernardini & Pirozzoli (2011) who reported the onset of AM effects in a DNS of a compressible turbulent boundary layer at Re_τ as low as 400.

6.2. *Principal component analysis*

With the presence of AM effects clearly established via both single- and two-point AM correlation coefficients, this physics is leveraged to achieve a physics-based model of higher-order statistics of all Reynolds stress components in smooth- and rough-wall flow. The anisotropy of wall turbulence results in non-zero correlation between the streamwise and wall-normal velocity components which represents the Reynolds shear stress. While the predictive work of Mathis *et al.* (2011) and Talluru *et al.* (2014) focused exclusively on the normal components of the Reynolds stress tensor, Agostini & Leschziner (2016) and Yin *et al.* (2018) have proposed models to predict the joint probability density functions (PDFs) of (u', v') and (u', w'). To model these anisotropies in a similar manner, principal component analysis (PCA), a tool often used to study the dynamics of turbulent coherent motions (Sirovich 1987), is exploited herein to account for such effects to predict off-diagonal terms of the Reynolds stress tensor. The PCA method is commonly used as a tool in studying large and complex sets of data that are generally correlated, to reveal the underlying relations and hence allow interpretations that would not be ordinarily possible. In this regard, PCA is a statistical procedure that transforms the original set of variables into a new set of linearly uncorrelated variables, termed the principal components. Geometrically, this transformation can be understood as rotating the original axes and the velocity fluctuations along a new coordinate system aligned with the principal components. By definition, the principal components are orthogonal to each other and ordered from the largest to the smallest correlation magnitude.

The application of PCA in turbulent channel flow is simplified as only the streamwise and wall-normal velocity fluctuations, u' and v', are correlated (the one-point correlations of w' with u' and v' are zero in turbulent channel flow; higher-order moment predictions of w' are postponed to the next section). Consider the linear transformation defined by

$$y = \begin{bmatrix} \xi \\ \eta \end{bmatrix} = \begin{bmatrix} c_{11} & c_{12} \\ c_{21} & c_{22} \end{bmatrix} \begin{bmatrix} u' \\ v' \end{bmatrix} = Cx, \qquad (6.12)$$

where $y = [\xi, \eta]^T$ represents the set of principal components, $x = [u', v']^T$ is the set of original velocity components, and C is a unitary rotation matrix (x and y in this section should not be confused with coordinate directions). We assume that ξ and η represent the first and second principal components, respectively. If we denote Σ_x and Σ_y as the covariance matrices of x and y, respectively, then they are related by the matrix C as

$$\Sigma_y = C\Sigma_x C^T. \qquad (6.13)$$

Let (λ_1, e_1), (λ_2, e_2) be the eigenvalue–eigenvector pairs of the covariance matrix Σ_x, where $\lambda_1 \geqslant \lambda_2 \geqslant 0$. The first step of PCA (Johnson & Wichern 2014) is to diagonalize the covariance matrix of the original velocity components Σ_x as

$$\Sigma_x = Q\Lambda_x Q^T, \qquad (6.14)$$

where Q denotes the orthogonal matrix whose columns are the eigenvectors e_1 and e_2, while Λ_x is the diagonal matrix with eigenvalues λ_1, λ_2 along the main diagonal. It is identified that

$$C = \begin{bmatrix} c_{11} & c_{12} \\ c_{21} & c_{22} \end{bmatrix} = \begin{bmatrix} e_1 & e_2 \end{bmatrix}^T = Q^T, \qquad (6.15)$$

and

$$y = Q^T x. \qquad (6.16)$$

Note that the original velocity components can be recovered by transforming the principal components back according to $x = Qy$.

The distributions of (u'^+, v'^+) for both smooth- and rough-wall flow are illustrated in figure 11 at four wall-normal locations. These scatter plots illustrate differences in the intensity of coupled u' and v' events between smooth- and rough-wall flow, particularly in the near-wall region where roughness enhances the intensity of these velocity fluctuations and thus their contributions to the Reynolds shear stress. With increasing wall-normal position, these differences between smooth- and rough-wall flow subside. As noted above, the principal components in this plane are obtained by projecting the original velocity components onto the principal axes denoted by solid (smooth) and dashed (rough) lines in the scatter plots. Therefore, it is readily seen that the distribution of the principal components can be obtained by rotating the original distribution to the new coordinate system formed by the principal axes. While the principal components of smooth- and rough-wall flow presented here show slight deviations, the differences for all flow cases can be quantified by calculating the angle between the new coordinate system aligned with the principal components and the original coordinate system, denoted by ϕ, measured in the clockwise direction with respect to the streamwise direction. Then (6.15) is simply,

$$Q^T = C = \begin{bmatrix} \cos\phi & -\sin\phi \\ \sin\phi & \cos\phi \end{bmatrix}. \qquad (6.17)$$
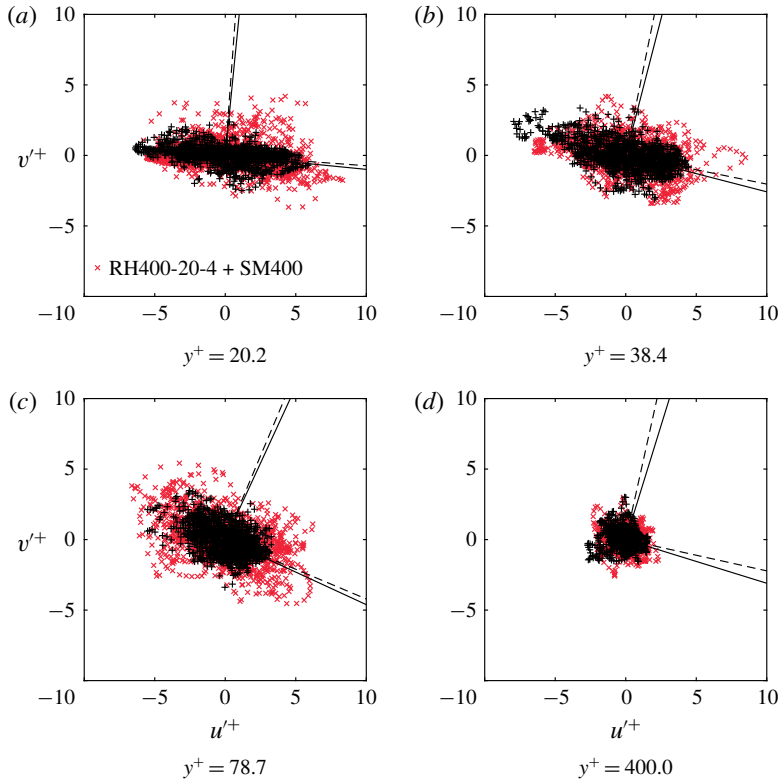
FIGURE 11. (Colour online) Distribution of (u'^+, v'^+) at four wall-normal positions. Solid lines denote principal axes for SM400; dashed lines denote the principal axes for RH400-20-4.

Figure 12 presents the angle $\phi(°)$ as a function of wall-normal position for all flow cases. The angle varies almost linearly with wall-normal distance, reaching approximately $20°$ near the centre of the log region. In the rough-wall cases, the angle of rotation for closely packed roughness elements ($d/k = 2$ case) is consistently reduced for all wall-normal positions as reflected in the RH400-20-2 trends. For the cases with larger element spacings ($d/k = 3$–4), however, the magnitude is slightly larger than the smooth-wall cases near the roughness crest. Of note, all rough-wall cases approach the present $Re_\tau = 400$ smooth-wall trends in the outer layer, indicative of outer-layer similarity outside the roughness sublayer. However, the higher Re smooth-wall flow of Hoyas & Jiménez (2006) has a lower value of ϕ in the log layer, indicating that this angle has Re dependence. The effect of Re on PCA clearly deserves more scrutiny.

7. Generalized predictive inner–outer interactions model

As noted earlier, Mathis *et al.* (2011) proposed a model to predict statistics of the streamwise velocity fluctuations in the near-wall region based on measurements of large-scale velocity signals in the outer layer where the model is calibrated. The mathematical formulation of the model is given by

$$\{u'^+(y^+)\}_p = u^*(y^+)\{1 + \beta u'^+_{OL}(y^+_O, \theta_L)\} + \alpha u'^+_{OL}(y^+_O, \theta_L), \tag{7.1}$$
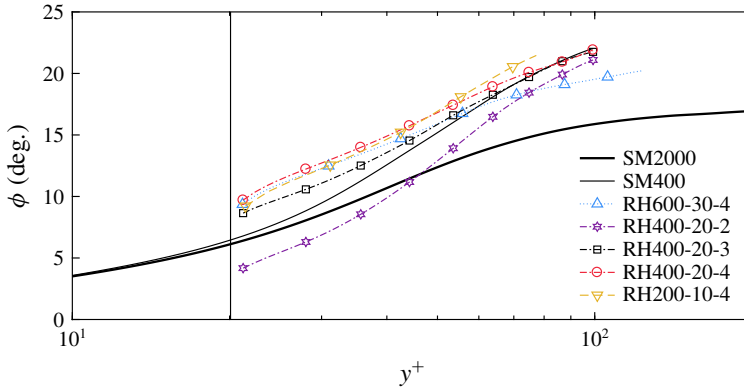
FIGURE 12. (Colour online) Angle of rotation of the principal axes of (u'^+, v'^+) for the smooth- and rough-wall cases. Vertical line denotes the location of the roughness crest $k^+ = 20$.

where $\{u'^+(y^+)\}_p$ is the predicted fluctuating velocity signal in the near-wall region, $u^*(y^+)$ is the universal signal that would exist if no AM effects were imparted by the outer-layer, large-scale signal, and the constants α, β and θ_L are determined while determining the universal signal. To calibrate the predictive model, two-point simultaneous sampling of data is typically performed for a range of wall-normal positions close to the wall (traversed vertically) with a reference wall-normal position in the outer region (fixed). This reference location, y_O^+, is generally not important as long as it resides in the log region. Note that in Mathis *et al.* (2011), the wall-normal locations were selected based on the empirical relation $y_O^+ = 3.9Re_\tau^{1/2}$ which corresponds approximately to the centre of the log region. The reference locations herein were chosen slightly further from the wall than that calculated by the empirical relation to reduce the influence of roughness on the log region for the lower-*Re* cases by ensuring that the outer position always sat outside the roughness sublayer. This reference location is used for the evaluation of the model (7.1) for all surface cases; the y_O^+ for each case is listed in table 3.

For large *Re*, the outer-layer, large-scale signals impart a strong 'footprint' on the small-scale activities near the wall. This effect is understood as superimposing low-wavenumber signatures by the outer large-scale structures on the near-wall fluctuating signals. Therefore, one expects to see certain correlations between the inner and outer large-scale components of the velocity signals. The large-scale components are obtained by filtering the synchronized fluctuating signals at the inner and outer planes with the same cutoff wavenumber used previously ($\kappa_c = 2\pi/h$). Then, the maximum cross-correlation between the two filtered large-scale signals is determined corresponding to the largest influence on the near-wall cycles imposed by the large-scale structures residing in the log region. For spatial signals, the correlation is further averaged in the spanwise direction to ensure statistical convergence. The superposition coefficient, α, is determined as the maximum of the cross-correlation between the two large-scale components, while the mean inclination angle of the large-scale structures, θ_L, is based on the streamwise offset $\Delta x_m/h$ associated with the peak cross-correlation. Using α and θ_L obtained as part of the calibration process, one can remove the footprint of the outer large-scale signal on the near-wall, small-scale flow, resulting in the de-trended signal, $u_d'^+(y^+)$, given by

$$u_d'^+(y^+) = \{u'^+(y^+)\}_c - \alpha u_L'^+(y_O^+, \theta_L) = u^*(y^+)[1 + \beta u_L'^+(y_O^+, \theta_L)]. \qquad (7.2)$$

Here, $\{u'^+(y^+)\}_c$ is the fluctuating velocity signal used for calibration and $u_L'^+(y_O^+, \theta_L)$ is the filtered outer large-scale signal shifted in the streamwise direction by an amount that corresponds to θ_L. With α, θ_L and $u_d'^+$ across the channel now known from this analysis, the universal signal u^* and the constant β can be determined from the de-trended signal by iterating values of β such that the degree of AM of the universal signal u^* is zero. Mathematically, this implies that given β, one must determine the signal u^* using (7.2) such that $AM\{u^*\} = 0$, where the coefficient of AM is calculated with respect to $u_L'^+(y_O^+, \theta_L)$. Hence, the universal signal represents the near-wall, small-scale signal with minimal influence from the outer-layer large-scale motions. Mathis *et al.* (2011) compared the universal signal calibrated by measurements in a turbulent boundary layer at $Re_\tau = 7300$ to a channel flow at $Re_\tau = 1000$ and found reasonable agreement between them. They therefore argued that the behaviour of a universal signal follows the low-*Re* flow in which the large-scale influence is weak. In this regard, β represents a measure of the degree to which small-scale turbulence is being modulated by the outer large-scale events. Thus, one would expect that β would share similar wall-normal trends as the two-point AM correlation coefficients.

The predictive model in (7.1) is established once u^* and the constants α, θ_L and β are determined across the inner region. The effectiveness and robustness of the model can be validated by examining the predicted small-scale signal according to (7.1). Note that in the calibration process, the filtered outer large-scale velocity signal, $\{u_L'^+(y_O^+, \theta_L)\}_c$, is extracted from the lower wall of the turbulent channel to obtain the model constants and universal signal. During the validation process, the input large-scale velocity signal, $\{u_L'^+(y_O^+, \theta_L)\}_p$, is obtained from the opposite wall at the reference wall-normal location (given in table 3) and spatially filtered with the same cutoff wavenumber as in the calibration process. Then, the filtered outer large-scale signal is shifted in the streamwise direction to account for the inclination angle θ_L associated with the universal signal u^* at each y^+ in the inner region. In general, the large-scale signal used for prediction is not necessarily synchronized with the corresponding universal signal obtained during calibration. Hence, by switching the Fourier phases of the outer large-scale signal used for calibration, $\{u_L'^+(y_O^+, \theta_L)\}_c$, with the one used for prediction, $\{u_L'^+(y_O^+, \theta_L)\}_p$, without altering the spectral density of the individual signal, one obtains the synchronized large-scale signal. Finally, the prediction of the near-wall, small-scale signal is readily obtained using (7.1). Further details of this method can be found in Mathis *et al.* (2011).

7.1. *Predictions of u' and v'*

While the original model, i.e. (7.1), proposed by Mathis *et al.* (2011), focused on predicting the statistics of u', it is possible to extend the model to other velocity components to make predictions of the full Reynolds stress tensor. Figure 13(*a,c,e*) compares the statistics of the Reynolds stresses calculated from DNS (lines) against those predicted by the original model (open symbols), where the outer large-scale signal u' is used for the calibration and prediction of both u' and v' in the near-wall region. Note that during the calibration for v', the constants are determined using the near-wall large-scale components of v'. It is also found that the superposition coefficient for v' reaches only approximately 0.6 close to the reference location, as opposed to 1.0 for u'. It is not surprising that the predictions of the streamwise Reynolds stress, $\overline{u'^2}$, agree well with that calculated from DNS for both smooth and rough-wall flows. For the wall-normal, $\overline{v'^2}$, and shear, $\overline{u'v'}$, stresses, however, the statistics are over-predicted by the original model as the reference plane is
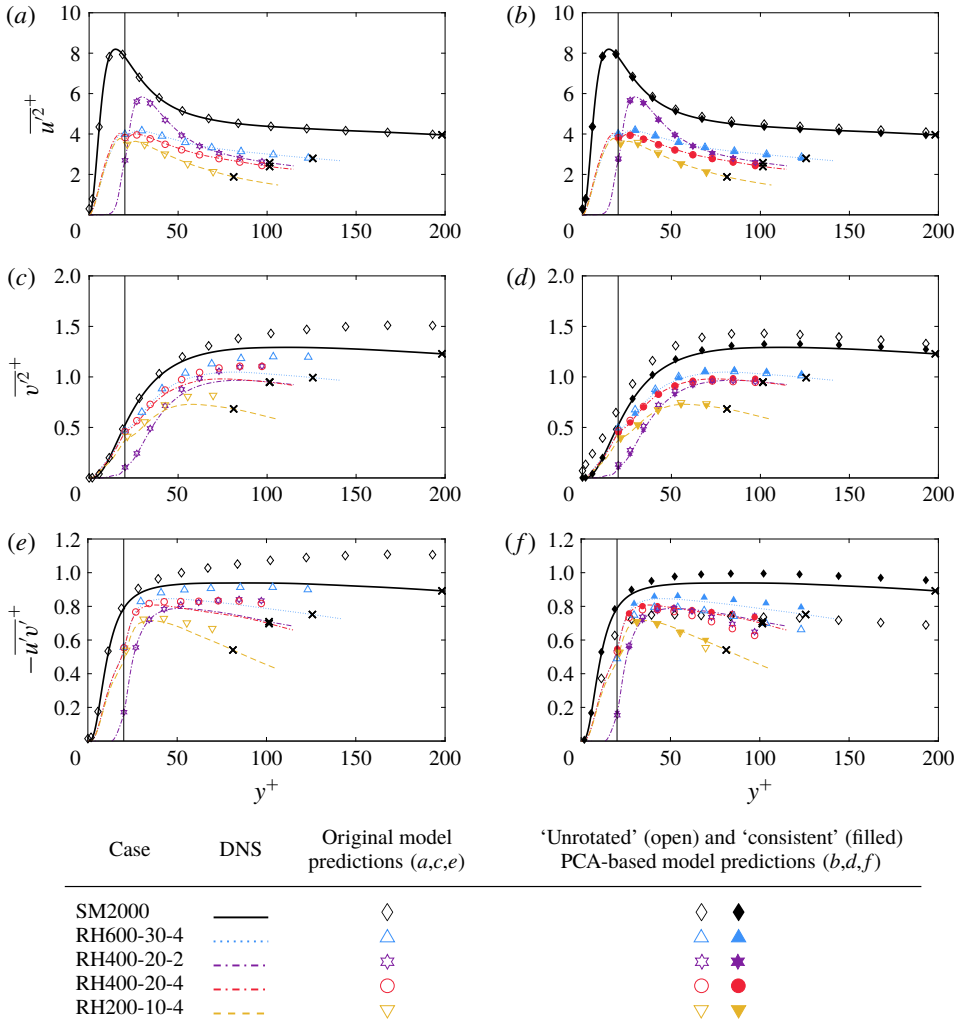
FIGURE 13. (Colour online) Predictions of the Reynolds stresses for the smooth- and rough-wall cases involving u' and v' compared with the actual statistics from DNS. (a,c,e) Original model of Mathis *et al.* (2011) (7.1); (b,d,f) PCA-adapted models using $u_{OL}'^+$ (unrotated PCA-adapted model; open symbols) and the outer large-scale $\xi_{OL}'^+/\eta_{OL}'^+$ (consistent PCA-adapted model; filled symbols). Symbol $\times$ marks the reference location where the large-scale signal is extracted. Vertical lines denote the location of the roughness crest $k^+ = 20$.

approached. Jiménez & Hoyas (2008) used spectral analysis to show that the presence of large-scale signatures with substantial energy are present in the premultiplied spectra of u' all the way from very near the wall to the top of the flow, a feature that represents the attached eddies whose dimensions scale well with the distance from the wall. Instead, spectra of v' and cospectra of $u'v'$ lack most of the energy carried by the long-wavelength structures residing in the outer layer, and thus embody the effects of detached eddies. The notion of attached and detached eddies, based on Townsend's attached-eddy hypothesis (Townsend 1976), can be related to the

predictive model in the sense that the outer large-scale information used as input in the model correlates better with u' rather than v'. This is seen in figure 13(*c,e*) with larger errors as the reference position is approached, since the outer layer is populated with more large-scale structures. Very recently, Yin *et al.* (2018) suggested that, while predicting the statistics of v' is accurate via the modulation effect embodied in the outer large-scale u', the superposition constants should be determined by the outer large-scale v'. Following this idea, we have proposed an alternative model that calibrates each velocity component using the corresponding outer large-scale signal and compared to the model using only the large-scale u'. The predicted statistics are shown in appendix C and it is observed that the statistics of v' are improved at higher *Re* with the alternative model but the correlations between u' and v' are still poorly reproduced.

Although the performance of the original model is limited by how well the outer large-scale signals are correlated with near-wall velocity signals, incorporating PCA to the model formulation allows one to make more robust predictions of the statistics for the Reynolds stresses associated with u' and v'; at least, for the modest *Re* we can effectively explore with the current DNS. Since the principal components are uncorrelated by construction, the modelling challenge is reduced to applying the analysis of AM to the principal components (ξ' and η') themselves and to independently calibrating the predictive inner–outer model. Doing so yields two sets of calibrated coefficients and universal signals for the two principal components, respectively. Then, the predicted near-wall fluctuating principal components are readily obtained in analogy to (7.1), e.g.

$$\{\xi'^+(y^+)\}_p = \xi^*(y^+)\{1 + \beta_\xi \xi_{OL}'^+(y_O^+, \theta_{L\xi})\} + \alpha_\xi \xi_{OL}'^+(y_O^+, \theta_{L\xi}), \tag{7.3}$$

$$\{\eta'^+(y^+)\}_p = \eta^*(y^+)\{1 + \beta_\eta \eta_{OL}'^+(y_O^+, \theta_{L\eta})\} + \alpha_\eta \eta_{OL}'^+(y_O^+, \theta_{L\eta}). \tag{7.4}$$

From (6.12), the predicted velocity fluctuations are obtained by (dropping subscript p for simplicity)

$$\left. \begin{aligned} u'(y^+) &= c_{11}(y^+)\xi'(y^+) + c_{21}(y^+)\eta'(y^+), \\ v'(y^+) &= c_{12}(y^+)\xi'(y^+) + c_{22}(y^+)\eta'(y^+), \end{aligned} \right\} \tag{7.5}$$

where the coefficients c_{ij} are obtained by calculating the eigenvectors of the covariance matrix at each wall-parallel plane near the wall, i.e. (6.15), of the velocity signals u' and v' extracted from the DNS data. Therefore, the Reynolds stresses can now be predicted according to

$$\left. \begin{aligned} \overline{u'^2} &= c_{11}^2 \overline{\xi'^2} + c_{21}^2 \overline{\eta'^2}, \\ \overline{v'^2} &= c_{12}^2 \overline{\xi'^2} + c_{22}^2 \overline{\eta'^2}, \\ \overline{u'v'} &= c_{11}c_{12} \overline{\xi'^2} + c_{21}c_{22} \overline{\eta'^2}. \end{aligned} \right\} \tag{7.6}$$

Note that the $\overline{\xi'\eta'}$ term does not appear in the expressions above since the principal components are orthogonal to each other by definition and this cross-correlation is thus zero.

The filled symbols in figure 13(*b,d,f*) represent the Reynolds stresses predicted using the principal components formulation described in (7.3) and (7.4), compared against the statistics calculated from DNS (lines). Overall, the predictions are in excellent agreement with the simulations for both smooth-wall (even in the higher *Re* simulation of Hoyas & Jiménez (2006)) and the present rough-wall cases, including
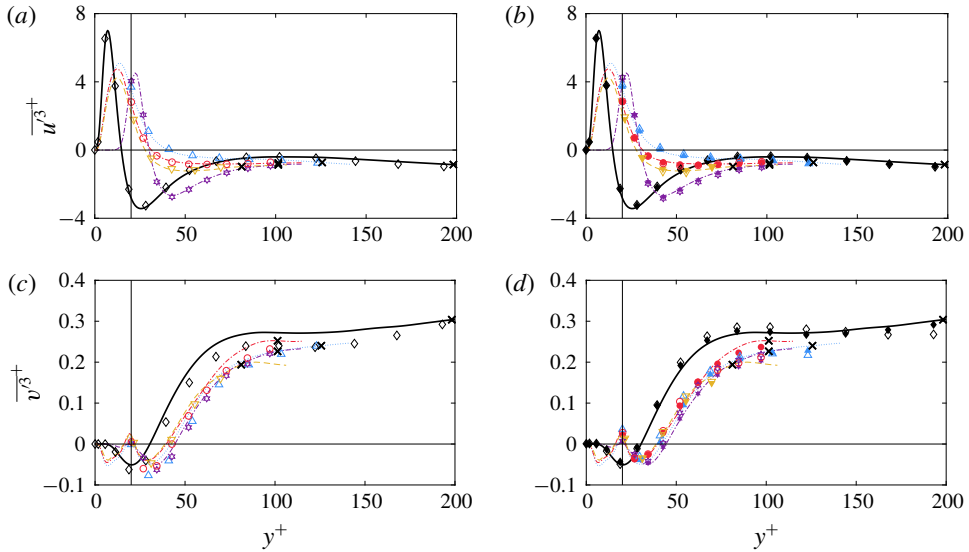
FIGURE 14. (Colour online) As in figure 13, but for third-order statistical moments.

$\overline{v'v'}$, and $\overline{u'v'}$. Recall that the principal components are obtained by rotating the axes of u' and v' to the principal axes. Consequently, the large-scale information originally carried by u'^+_{OL} is effectively transferred to both principal components. Therefore, this PCA-adapted model yields more consistent correlations between inner and outer signals compared to the original model as it embodies anisotropies inherent in the flow, resulting in improved predictions of statistics associated with v'.

In the formulation of the PCA-adapted model, the outer large-scale signals can be rotated by an angle that is either consistent with the outer principal components or with the near-wall principal components, e.g. $\phi(y^+_O)$ or $\phi(y^+)$, respectively. These two sets of predictions are indistinguishable and are therefore not shown. The solid symbols in figure 13(b,d,f) as discussed above correspond to rotating the near-wall and outer-layer signals according to their local principal components – which can be quite different – so this formulation is termed the 'consistent' PCA-adapted model. Alternatively, one could still utilize the PCA-based model but instead leave the outer large-scale signals unrotated. Thus, the outer large-scale component of u' would be used to calibrate and predict the near-wall principal components ξ' and η', respectively, and is termed the 'unrotated' PCA model. These results are also included in figure 13(b,d,f) and are represented by the open symbols. Interestingly, this variant of the model accurately predicts $\overline{u'u'}$ well, but results in considerable differences in other components with Re. These differences are primarily due to poor correlation between the outer large-scale signal, u', and the near-wall second principal component, η'.

The efficacy of the PCA-adapted models is further investigated by examining higher-order statistics involving u' and v', as shown in figures 14–17. These higher-order predictions are obtained in a similar fashion as the Reynolds stresses. In particular, third- (figures 14 and 16) and fourth-order (figures 15 and 17) moments, including cross-correlation terms, are computed using the original model of Mathis *et al.* (2011) (panels *a* and *c* of each figure) as well as both the consistent and unrotated PCA models (panels *b* and *d* of each figure), with the former represented
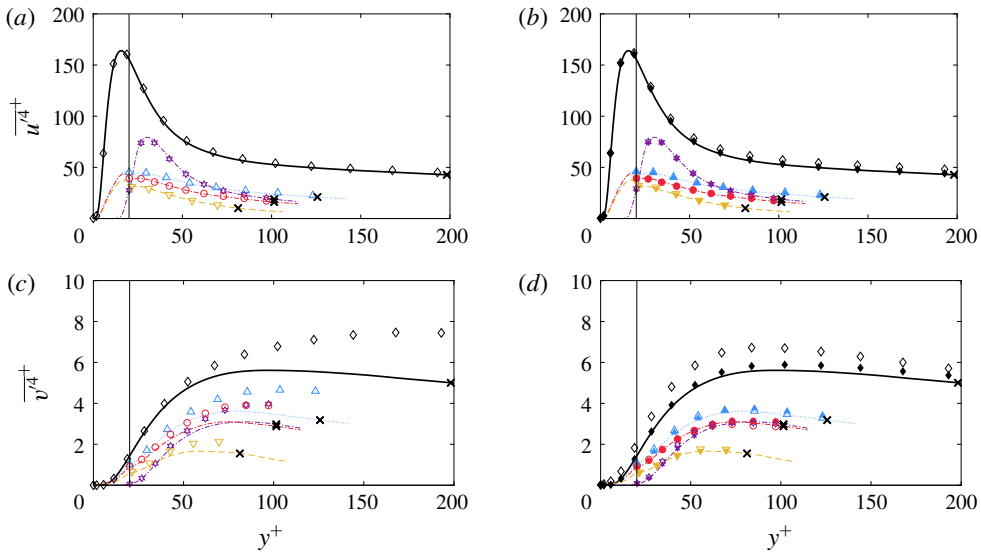
FIGURE 15. (Colour online) As in figure 13, but for fourth-order statistical moments.

by solid symbols and the latter by open symbols. As one would expect, predictions of $\overline{u'^3}^+$ and $\overline{u'^4}^+$ by all three models agree very well with the original statistics for the smooth- and rough-wall cases. However, as with $\overline{v'v'}^+$, the original model poorly predicts $\overline{v'^3}^+$ and $\overline{v'^4}^+$ compared to the PCA-adapted models, although the consistent version provides the most accurate reconstruction of these v' statistics. Interestingly, all three models perform equally well in predicting the third-order cross-correlation ones. However, similar to the Reynolds shear stress, the fourth-order cross-terms are severely over-predicted by the original model and notably over-predicted by the unrotated PCA-based model, while the consistent PCA-based model accurately reconstructed these statistics. Finally, since the consistent PCA-adapted model is formulated for the specific purpose of accurately predicting near-wall statistics based on outer-layer information, it is not surprising to note small deviations in some of the higher-order statistics in the outer region for this model. Despite these outer-layer deviations, the consistent PCA-adapted model performs very well in predicting near-wall behaviour based on outer-layer flow information.

7.2. *Predictions of w'*

The previous section was devoted to the prediction of joint statistics of u' and v' owing to their interdependence in wall turbulence. As shown in §6.1 (figure 10), one can observe an important AM correlation between the near-wall w' and outer-layer u'. Spectral analysis of w' (Jiménez & Hoyas 2008) has shown that long-wavelength signatures are present over the entire flow thickness, although not as strong as u', implying that w' is also an attached variable in the spirit of Townsend's attached eddy hypothesis (Townsend 1976).

These observations, while important, are not sufficient to formulate a useful predictive model for statistics of w'. From the Reynolds stress balance equations, the only mechanism of production of w' fluctuations is the pressure strain, where
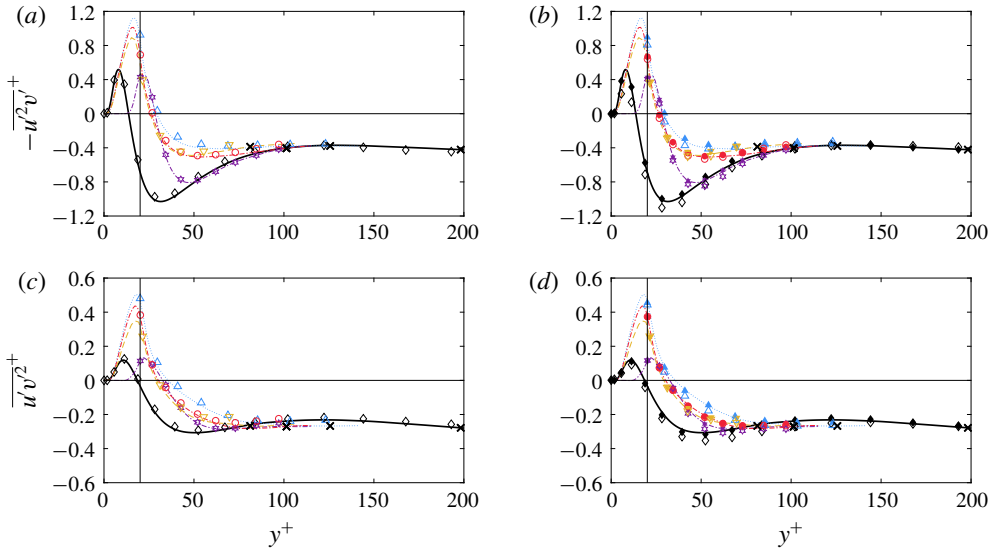
FIGURE 16. (Colour online) As in figure 13, but for the third-order cross-correlated statistical moments.

it acts as a sink for u' and a source for v' and w'; the net pressure strain, or the pressure dilatation, being zero in incompressible flow. This consequence complicates the situation because, for w', the transport field (the source of its energy) is the pressure, which has long-range interactions and is difficult to model. Nevertheless, it is known that p' derives its intensity from u', although it is not known which region in space and wavenumber predominantly contribute to it. Since near-wall statistics of u' can be inferred from the outer large-scale u'_{OL}, a major conclusion of AM, it make sense to directly consider the relationship between the near-wall w' and the outer-layer u' in more detail. To do so, we consider the two-point correlation between the near-wall w' and the outer-layer u' in the x–z plane with a two-point separation vector $(\Delta x^+, \Delta z^+)$. This x–z correlation between w' on a near-wall plane (y_i^+) and u' on an outer-layer plane (y_O^+) is given by

$$\rho_{iO}(\Delta x^+, \Delta z^+; y_i^+; y_O^+) = \frac{\overline{w'^+_{iL}(x^+, z^+; y_i^+)\ u'^+_{OL}(x^+ + \Delta x^+, z^+ + \Delta z^+; y_O^+)}}{\sqrt{\overline{w'^+_{iL}(x^+, z^+; y_i^+)^2}}\sqrt{\overline{u'^+_{OL}(x^+, z^+; y_O^+)^2}}}. \quad (7.7)$$

Figure 18 presents iso-contours of this two-dimensional, off-plane, two-point correlation coefficient for the smooth-wall case SM400 in comparison with the higher-*Re* smooth-wall case, SM2000. The inner plane is located at $y_i^+ = 20$ in both cases, while the outer reference location is $y_O^+ = 100$ for SM400 and $y_O^+ = 200$ for SM2000, respectively. An anti-symmetric correlation between w'_{iL} and u'_{OL} is noted in the x–z plane. Here the positive/negative peaks are no longer located along the x-axis where $\Delta z^+ = 0$, but with an offset in the spanwise direction whose distance increases with *Re*. This spanwise offset is similar to the experimental results reported by Volino *et al.* (2007) who also found that u' and w' in the same wall-parallel planes are correlated on both spanwise sides. The observed spanwise offset implies that, in
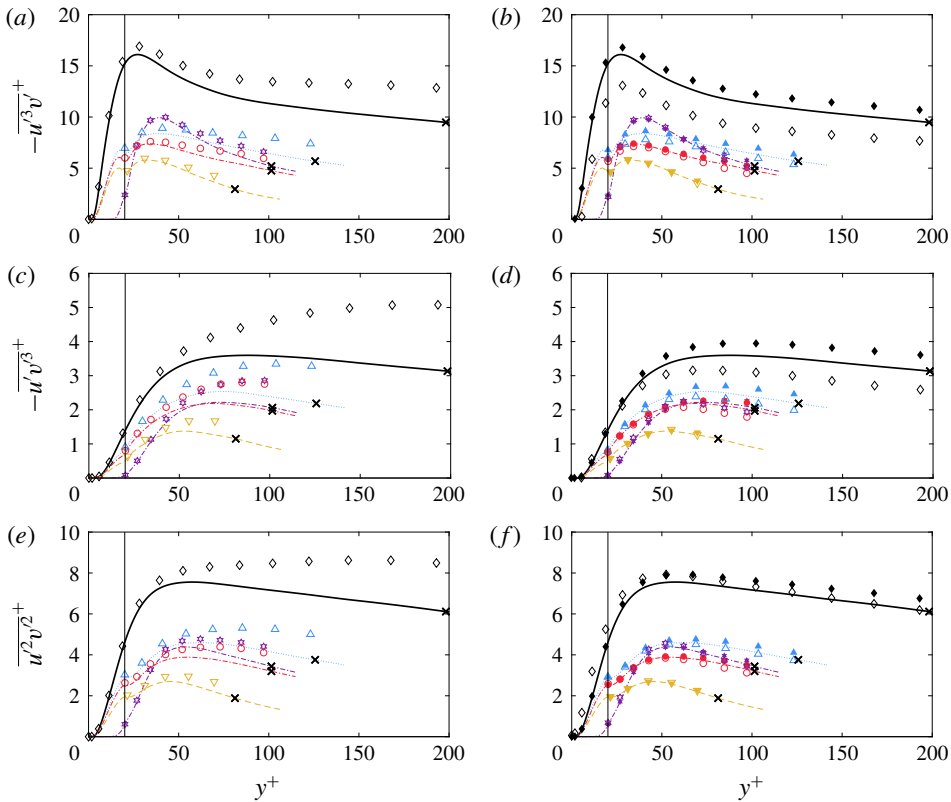
FIGURE 17. (Colour online) As in figure 13, but for the fourth-order cross-correlated statistical moments.

order to extend the original model, equation (7.1), for w' statistics, one must calibrate the velocity component w' with both a streamwise and a spanwise shift. Thus, the original model can be modified as

$$\{w'^+(y^+)\}_p = w^*(y^+)\{1 + \beta_w u'^+_{OL}(y^+_O, \theta_x, \theta_z)\} + \alpha_w u'^+_{OL}(y^+_O, \theta_x, \theta_z), \qquad (7.8)$$

where θ_x and θ_z are the inclination angles in the streamwise and spanwise directions, respectively. For simplicity, w'^+ is calibrated with u'^+_{OL} and not with ξ'^+_{OL} or η'^+_{OL} as the rotation angle of PCA is only relevant when considering cross-interactions, like those between u' and v'. Equivalent results are obtained if ξ'^+_{OL} is used above instead.

Although both the positive and negative peaks shown in figure 18 can be used to calibrate the model, for simplicity, only the negative peak is used herein. However, equivalent results can be obtained if the positive peak is used. The magnitude of the superposition coefficient for all flow conditions is shown in figure 19. Unlike the trends generally observed for u', $|\alpha_w|$ reaches a peak value (less than 1) below the reference location and gradually diminishes further away from the wall. It is also seen that the superposition coefficient tends to grow as the Re increases. Overall, consistent trends are observed between the smooth- and rough-wall flows at the same Re, except that the peak values are increased and move closer to the reference location in the presence of roughness. Finally, the coefficient magnitude is reduced near the roughness
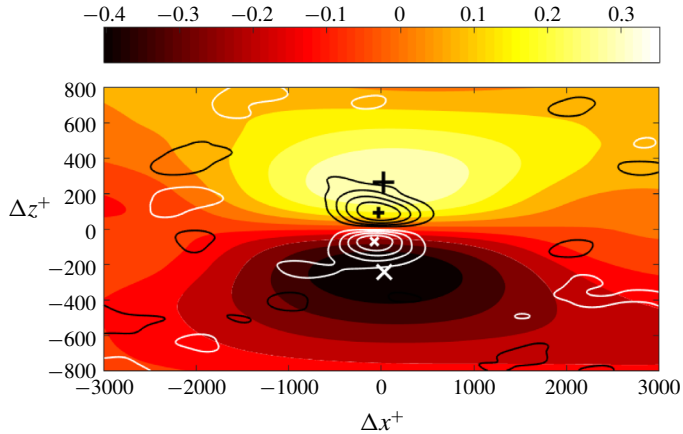
FIGURE 18. (Colour online) Two-point cross-correlation coefficient, $\rho_{iO}(\Delta x^+, \Delta z^+)$, between w_{iL} and u_{OL} in the x–z plane. Contour lines: case SM400 (dark lines: positive ρ_{iO}; light lines: negative ρ_{iO}) with increment/decrement of 0.2 times the peak values. Shaded contours: case SM2000 (light shade: positive ρ_{iO}; dark shade: negative ρ_{iO}). The outer plane is located at $y_O^+ = 100$ for SM400 and $y_O^+ = 200$ for SM2000. The inner plane is located at $y^+ = 20$ for both cases. Markers: '+' denotes the positive peak and '×' denotes the negative peak. Larger markers refer to the higher-*Re* case.
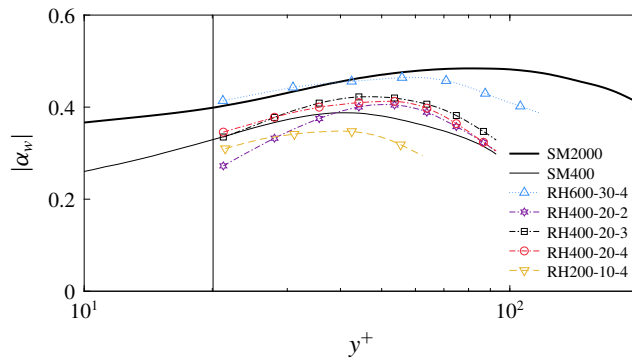
FIGURE 19. (Colour online) Superposition coefficient α_w (magnitude). Vertical line denotes the location of the roughness crest $k^+ = 20$.

crest with closely packed hemispheres compared to topographies with larger element spacings. Note that the superposition coefficients can be alternatively calibrated using the outer large-scale w' and the results and associated discussion can be found in appendix C.

Figure 20 shows the wall-normal evolution of the inclination angles θ_x and θ_z for w' in inner units. For the low *Re* smooth-wall flow (SM400), $w_{iL}'^+$ appears to lag $u_{OL}'^+$ in the streamwise direction near the wall. Away from the wall, however, $w_{iL}'^+$ slowly transitions to lead $u_{OL}'^+$ in the streamwise direction as it approaches the reference location. In particular, θ_x for the case SM400 increases from an acute angle of approximately 45° in the near-wall region to an obtuse one above $y^+ \approx 40$
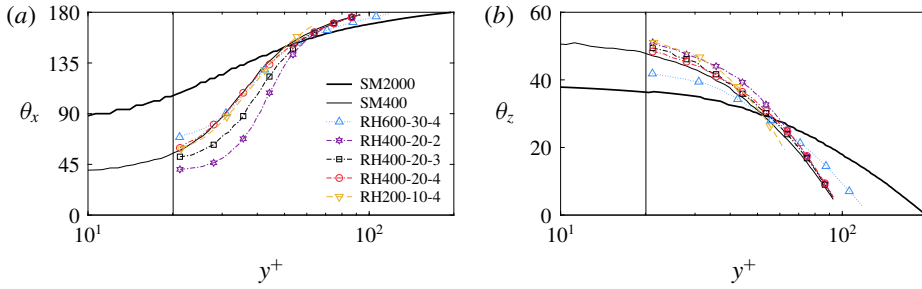
FIGURE 20. (Colour online) Inclination angles θ_x and θ_z for w'. Vertical line denotes the location of the roughness crest $k^+ = 20$.
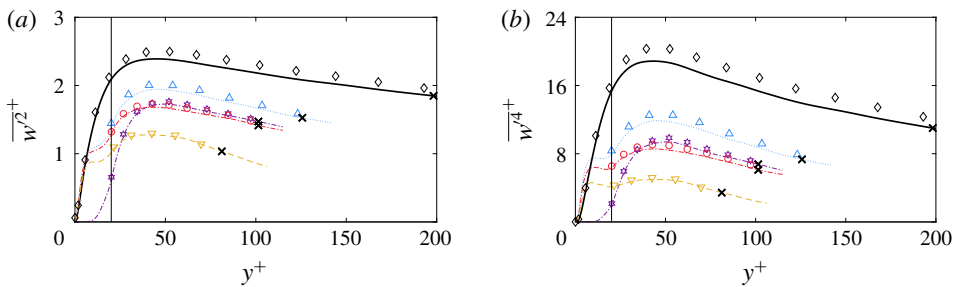

FIGURE 21. (Colour online) Predictions of (a) $\overline{w'^2}^+$ and (b) $\overline{w'^4}^+$ for the smooth- and rough-wall cases in comparison with the original DNS statistics. Symbol $\times$ marks the reference location where the large-scale signal is extracted. Vertical line denotes the location of the roughness crest $k^+ = 20$. Legend as in figure 13.

and eventually reaches $180°$ close to the outer reference location. At higher Re (SM2000), $w_{iL}'^+$ exhibits excellent synchronization with $u_{OL}'^+$ very close to the wall, but begins to lead $u_{OL}'^+$ with increasing wall-normal distance. Similar behaviours of θ_x are observed for the rough-wall cases; however, the Re trend shown in the smooth cases is not as clear in the rough cases, at least for the moderate Re studied herein. More interestingly, at the same Re, θ_x near the roughness crest is gradually reduced for narrowly spaced roughness elements, but is indistinguishable between the smooth- and rough-wall cases if the elements are sufficiently far apart. This behaviour can be explained by the lifting effect of fluid away from the wall owing to the presence of roughness elements. The spanwise inclination angle, θ_z, is reported in figure 20(b). Here, θ_z decreases as a function of y^+ from approximately $50°$ for the smooth-wall case SM400 and $40°$ for SM2000 close to the wall, to $0°$ near the reference plane. Unlike the trends observed in θ_x for the rough-wall cases, a Re trend is more apparent in θ_z while the effect of roughness-element spacing diminishes.

Figure 21 presents $\overline{w'^2}$ and $\overline{w'^4}$ using this modified model, equation (7.8), for both smooth- and rough-wall cases (note that $\overline{w'^3}$ is zero by symmetry). Both $\overline{w'^2}$ and $\overline{w'^4}$ predicted by (7.8) are in good agreement with the DNS results for all surfaces. As these results are the initial attempt to model w' statistics with streamwise and spanwise offsets, definitive trends with Re cannot be established owing to the relatively
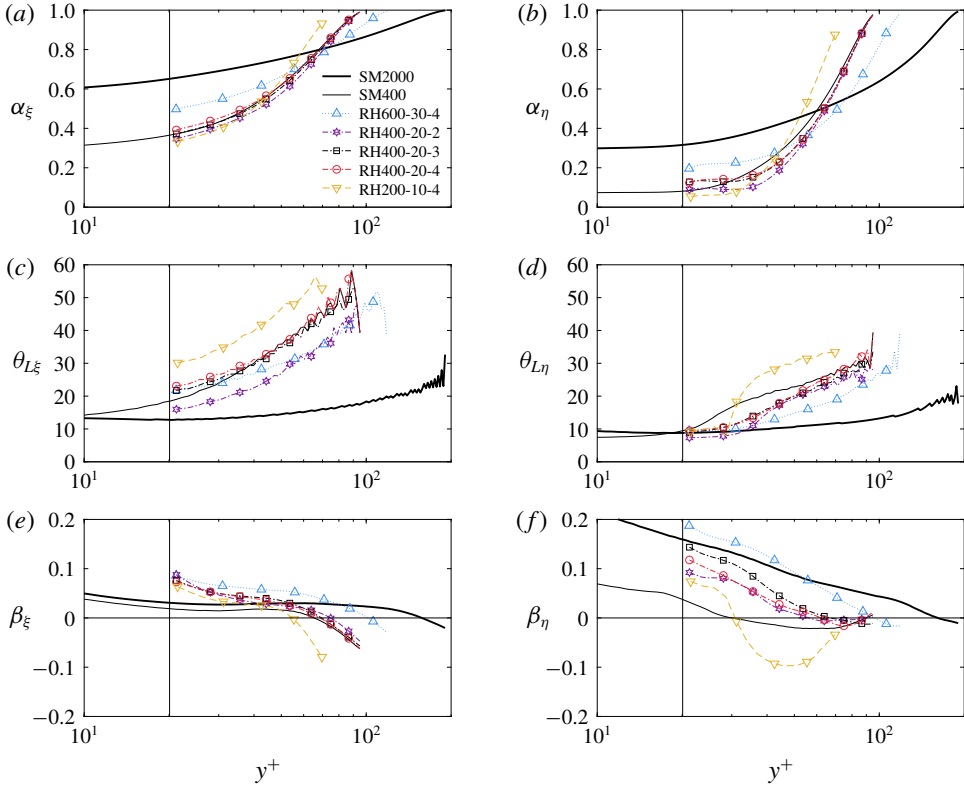
FIGURE 22. (Colour online) Superposition coefficient, α, inclination angle, θ_L, and modulation coefficient, β, for the smooth- and rough-wall cases. (*a,c,e*) First principal component, ξ'; (*b,d,f*) second principal component, η'. Vertical line denotes the location of the roughness crest $k^+ = 20$.

moderate *Re* studied herein. However, the present results are clearly encouraging from a modelling perspective.

7.3. *Model coefficients and universal signals in PCA form*

The 'consistent' PCA-based model presented herein predicts the behaviour of the principal components, ξ and η, rather than the velocities as in the original model of Mathis *et al.* (2011) as shown in (7.3) and (7.4). Therefore, each principal component will have an associated superposition coefficient, α, inclination angle, θ_L, and modulation coefficient, β. These modelling coefficients are shown as a function of y^+ in figure 22, where the solid vertical line denotes the location of roughness crests ($k^+ = 20$). For the first principal component, the superposition coefficient α_ξ increases in the near-wall region from approximately 0.3 for SM400 and 0.6 for SM2000, respectively, to 1 near the reference position. As α_ξ is a measure of large-scale phenomena, the agreement noted between the smooth- and rough-wall cases implies that it is relatively unaffected by the presence of roughness, with a slight enhancement near the roughness crest as the element spacing increases. However, given the same roughness height and spacing, α_ξ tends to grow with *Re*. Similar trends are observed for α_η, except for the lower magnitudes near the wall.
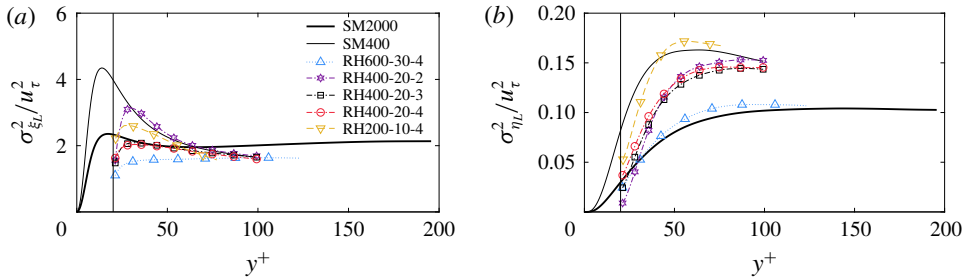
FIGURE 23. (Colour online) Amplitude of the large-scale signals based on PCA for the smooth- and rough-wall cases. (*a*) First principal component, ξ_L; (*b*) second principal component, η_L. Vertical line denotes the location of the roughness crest $k^+ = 20$.

The inclination angle for the first principal component, $\theta_{L\xi}$, varies slowly from $10°$ to $25°$ in the range $10 < y^+ < 200$ in the highest Re case, consistent with previous experiments (Mathis *et al.* 2011). For lower Re in both smooth- and rough-wall cases, however, this inclination angle increases with y^+, reaching approximately $60°$ close to the reference location. In addition, it is notable that roughness has no significant impact on $\theta_{L\xi}$, except for the case with closely packed hemispheres (RH400-20-2) where $\theta_{L\xi}$ is consistently reduced compared to the smooth-wall case owing to the mutual sheltering of roughness elements. For the second principal component, $\theta_{L\eta}$ grows slower compared to $\theta_{L\xi}$, reaching approximately $20°$ for the highest Re case and $30°$ for lower Re cases near the reference position. Roughly speaking, the behaviours of $\theta_{L\xi}$ and $\theta_{L\eta}$ are similar in the rough-wall cases, with the exception of the lowest Re case, where the latter drops rapidly within the roughness sublayer.

A comparison of the modulation coefficients β_ξ and β_η is also shown in figure 22. Roughness enhances both β_ξ and β_η in the near-wall region compared to the smooth-wall result. At $Re_\tau = 400$, roughness-element spacing appears to have a weak effect at best on β_ξ and β_η as the results for $d/k = 2$–4 show only small differences. In addition, β_ξ and β_η grow with Re, as β is another measure of the AM effect, which is the weakest in the $Re_\tau = 200$ case and strongest in the $Re_\tau = 600$ case among the rough-wall simulations. This effect seems to be stronger in β_η.

Note that the large-scale signals are the only terms in the predictive model that vary between the calibration and prediction processes. Thus, the correctness of the model depends significantly on the large scales themselves. If the amplitude of the large-scale signals are small compared to that of the universal signals, the agreement of the predictions reported herein might occur regardless of the correctness of the model. Therefore, the amplitude of the large-scale signals based on PCA are reported in figure 23 for the smooth- and rough-wall flows. For both principal components, it is shown that the amplitude of the large-scale signal approaches a constant value beyond $y^+ \approx 100$, consistent between the smooth- and rough-wall flows. Moreover, the amplitude of the large-scale signal decreases as the Re increases and is likely to reach an asymptotic limit at sufficiently high Re. This is expected as the separation of scales is difficult to achieve at low Re and hence some proportion of the moderate- to large-scale structures are counted as the large scales while low-pass filtering the velocity signals. In comparison with the amplitude of the universal signals shown in figure 24(*a,b*), the large scales of both principal components remain non-negligible near the wall above the roughness crest. Therefore, the changes in the large-scale
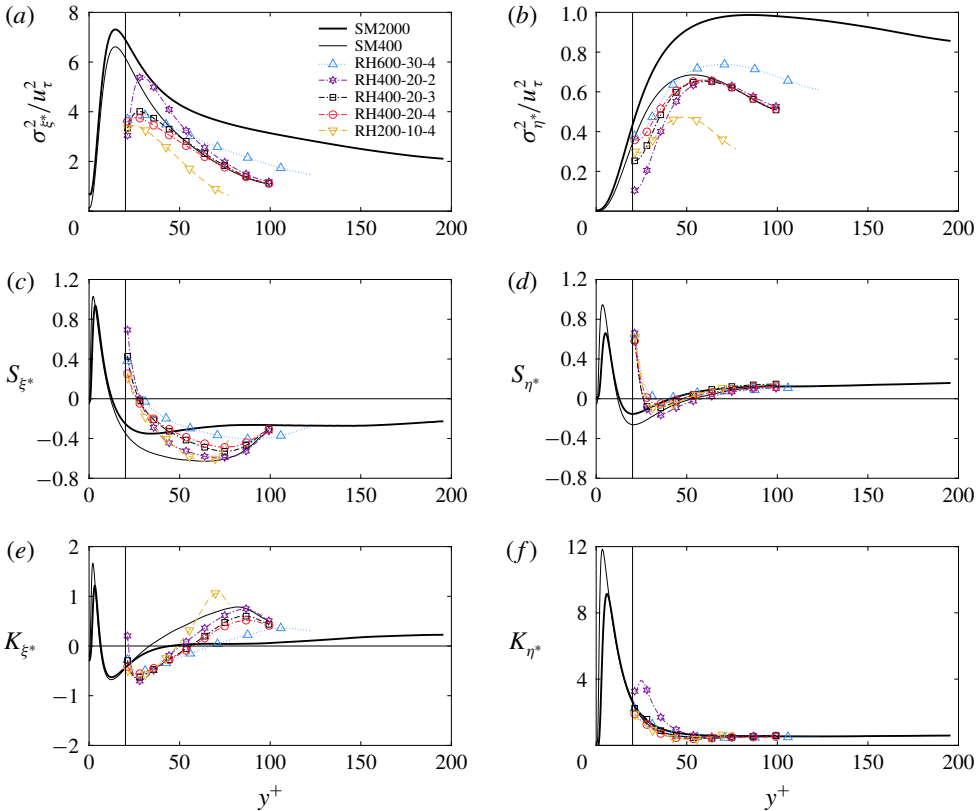
FIGURE 24. (Colour online) Statistical properties of the universal signals based on PCA for the smooth- and rough-wall cases. (*a,c,e*) First principal component, ξ^*; (*b,d,f*) second principal component, η^*. Vertical line denotes the location of the roughness crest $k^+ = 20$.

signals from the calibration to the prediction process have an impact on the predicted statistics based on the main model.

The effect of surface conditions on the variance, skewness and kurtosis (subtracted by 3) of the universal signals based on the principal components are shown in figure 24. The variance of the first principal component ξ^*, normalized by the friction velocity, demonstrates a strong reduction in the peak values near the roughness crest, compared to the smooth-wall cases. This reduction is stronger for 'k-type' roughness as reflected in the cases with $d/k = 3$–4 compared to 'd-type' roughness as in the case with $d/k = 2$ (closely packed hemispheres). Moreover, although all statistical properties of the first principal component are still *Re* dependent among the rough-wall cases, they show perceivable tendency towards the high *Re* limits in which the variance varies slowly while the skewness and kurtosis remain almost constant for $y^+ > 100$ for the smooth-wall flow at $Re_\tau = 2000$. Even better outer-layer consistency is noted in the statistics of the second principal component, η^*, where a similar tendency toward high *Re* trends is present for the variance as well as excellent collapse of skewness and kurtosis observed among all cases beyond $y^+ \approx 80$. From the perspective of modelling the inner–outer interactions in rough-wall flows, this outer-layer similarity means it is conceivable that the universal signals calibrated at sufficiently high *Re*, whether the surface is smooth or rough, can be used for reasonable predictions of
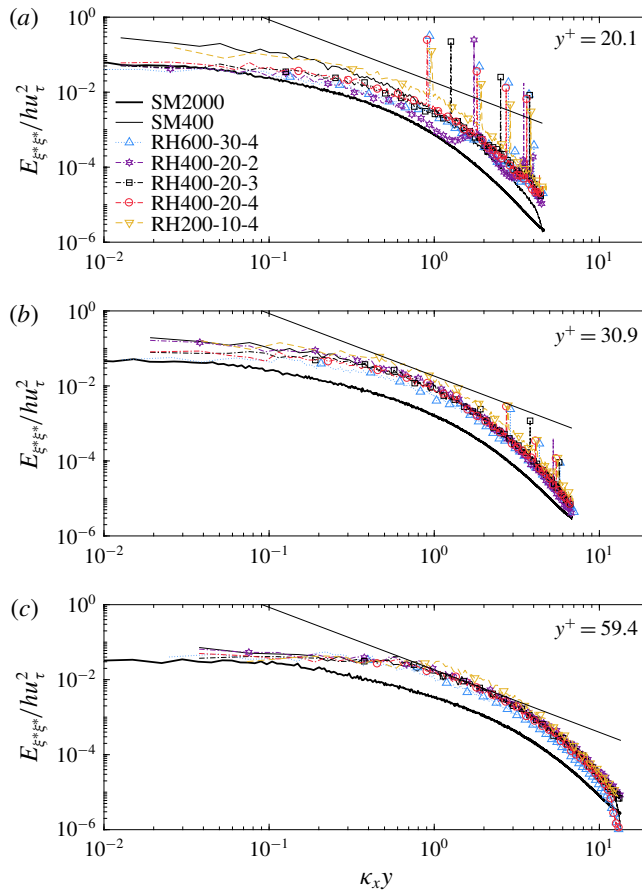
FIGURE 25. (Colour online) Energy spectra of the universal signals based on PCA at (*a*) $y^+ = k^+$, (*b*) $y^+ = 1.5k^+$ and (*c*) $y^+ = 3k^+$ for the smooth- and rough-wall cases. All spectra are normalized by the friction velocity, u_τ, and half-channel height, h.

the near-wall velocity signals outside the roughness sublayer based solely on the outer-layer large-scale information.

Energy spectra of the universal signals of the first principal component, $E_{\xi^*\xi^*}/hu_\tau^2$, at selected wall-normal positions are shown in figure 25. Very close to the roughness crest, at $y^+ = 20$, large spikes are noted in the spectra of the rough-wall flows. The location of these energy spikes is closely related to the streamwise wavelength characterizing the geometry of the rough surfaces. For example, the first peak for the case RH400-20-4 corresponds to the wavelength $\lambda = 0.349$, which is approximately equal to the separation between roughness elements ($\sqrt{3}d$ or $4\sqrt{3}k$) in the streamwise direction (see the inset of figure 2(*b*) for a graphical representation of the geometry). Additionally, a higher degree of energy content is found at large wavenumbers in the rough-wall flows coupled with a reduction in energy at low wavenumbers compared to the smooth-wall case. This behaviour is expected since the presence of roughness energizes the near-wall turbulence, likely through the shedding of energetic, small-scale, vortical motions that scale with the roughness height. As one moves away

from the wall, the effect of surface roughness is reduced, and, at $y^+ = 3k^+$, all energy spectra at $Re_\tau = 400$ collapse onto one another, indicating that the influence of roughness is restricted to the roughness sublayer that resides within a few roughness heights from the wall. This collapse of energy spectra for all surface conditions is useful as a guideline for modelling turbulence over rough surfaces.

8. Conclusions

Direct numerical simulations of turbulent channel flow over smooth and rough surfaces, the latter consisting of hexagonally packed array of hemispheres, were performed at $Re_\tau = 200$, 400 and 600. The normalized roughness height for all Re was fixed at $k^+ = 20$ while the distance between neighbouring roughness elements varied in the range $d/k = 2$–4. Profiles of the mean streamwise velocity reflect its expected downward shift owing to the enhancement in drag for all rough-wall cases compared to smooth-wall flow. Excellent agreement of the roughness function values was observed for all 'k-type' rough-wall flows, showing an effective dependence on k^+. However, the case with densely packed hemispheres, classified as 'd-type' roughness, showed a reduced downward shift compared to other rough-wall flows, owing to the sheltering effect generated between closely spaced roughness elements. In addition, the equivalent sand-grain roughness heights k_s^+ indicate that flows studied herein reside in the transitionally rough regime. Moreover, profiles of the Reynolds stresses show that the roughness significantly reduced the inner peak of the streamwise Reynolds normal stress in all rough-wall cases compared to the smooth-wall case. However, outside the roughness sublayer the Reynolds stresses of the rough-wall cases converge to the smooth-wall trends, supporting the occurrence of outer-layer similarity irrespective of the surface conditions and Re_τ.

These DNS data also afforded the opportunity to explore amplitude modulation of the small-scale, near-wall flow by the larger-scale, outer-layer motions in all three velocity components. The single-point AM correlation coefficients for all three velocity components demonstrate enhanced modulation within the roughness sublayer compared to the smooth-wall case, although this enhancement diminishes with increasing wall-normal position as the rough-wall AM results converge to the smooth-wall AM trend outside the roughness sublayer. This outer-layer consistency between the smooth- and rough-wall flows is yet another indication of outer-layer similarity in these flows as quantified through these inner–outer flow interactions.

In previous studies of smooth-wall turbulent boundary layers, Mathis *et al.* (2011) proposed a predictive inner–outer model using the concept of AM to investigate the statistical properties of streamwise velocity fluctuations. This model was applied herein to the smooth- and rough-wall cases, but extended to consider predictions of all velocity components. It was found that the calibration coefficient β closely resembles the two-point AM coefficient and the presence of roughness tends to enhance the modulation effect imparted by the outer-layer motions on the near-wall small-scale motions, with this effect growing stronger with increasing Re_τ.

The effect of anisotropy was also explored within the AM framework using principal component analysis. Constructing the predictive model based on the principal components of u' and v' yielded uncorrelated universal signals which enabled prediction of correlated velocity statistics. Although the statistical properties of the universal signals behave differently between 'k-type' and 'd-type' roughness in the near-wall region, similarity is preserved outside the roughness sublayer for $y > 3k$. Combining the universal signals derived from the principal components facilitated

predictions of not only the moments of u' and v' but also moments of cross-terms i.e. $\overline{u'v'}$, $\overline{u'^2v'}$ and $\overline{u'^2v'}$, etc. The efficacy of this approach was validated by comparing predictions of Reynolds stresses and higher-order moments in the near-wall region to the true statistics computed from the DNS. For all cases presented, predictions up to fourth-order moments, including moments between correlated variables, with the consistent PCA-adapted model showed superior agreement with the original statistics compared to models that do not embody anisotropy of the flow. As this model is constructed to accurately predict near-wall statistics based on outer-layer information, some deviations in these statistics was noted in the outer layer as the reference position was approached. Despite these outer-layer deviations, the model performs very well in predicting near-wall behaviour based on outer-layer flow information and thus holds great promise for near-wall modelling of rough-wall flows.

Furthermore, the AM effect was explored for the spanwise velocity fluctuations, w'. Development of an accurate predictive model of w' moments required not only a streamwise shift in the signal correlation but also a spanwise one as motivated by two-point correlations between spanwise and streamwise velocity fluctuations in the near-wall and outer regions, respectively. With this adaptation, the original predictive model was generalized to accurately predict near-wall statistics of w' based on the knowledge of the outer-layer u'.

Finally, acknowledging the fact that flow structures are strongly modified within the roughness sublayer, applying the predictive model presented herein to rough-wall flows requires a better understanding of outer-layer similarity at higher *Re*. Nevertheless, the results presented herein indicate that the consistent PCA-adapted model can yield accurate predictions of near-wall statistics at lower *Re*. Thus, a study of its efficacy at higher *Re* and for a broader spectrum of roughness parameters would allow its potential broader applicability to be assessed.

Acknowledgements

Appendix A. Two-point correlations of velocity fluctuations

The appropriateness of the computational domain size is demonstrated using the two-point autocorrelation coefficients of the velocity fluctuations in the streamwise and spanwise directions. The two-point autocorrelation coefficient is defined as

$$R_{u_i}(\Delta x; y) = \frac{\overline{u_i'(x + \Delta x, y, z)\ u_i'(x, y, z)}}{\sqrt{\overline{u_i'(x + \Delta x, y, z)^2}}\sqrt{\overline{u_i'(x, y, z)^2}}}, \quad i = 1, 2, 3, \quad \text{(A 1)}$$

with no summation over i. An analogous expression is used for the two-point autocorrelations as a function of Δz.

Figures 26 and 27 show the two-point autocorrelation coefficients of all velocity components in both smooth- and rough-wall cases at planes close to the roughness crest ($y^+ = 20$) and in the outer region ($y^+ = 350$), respectively. As seen in figures 26(*a*) and 26(*b*), the autocorrelation coefficients for the rough-wall case near
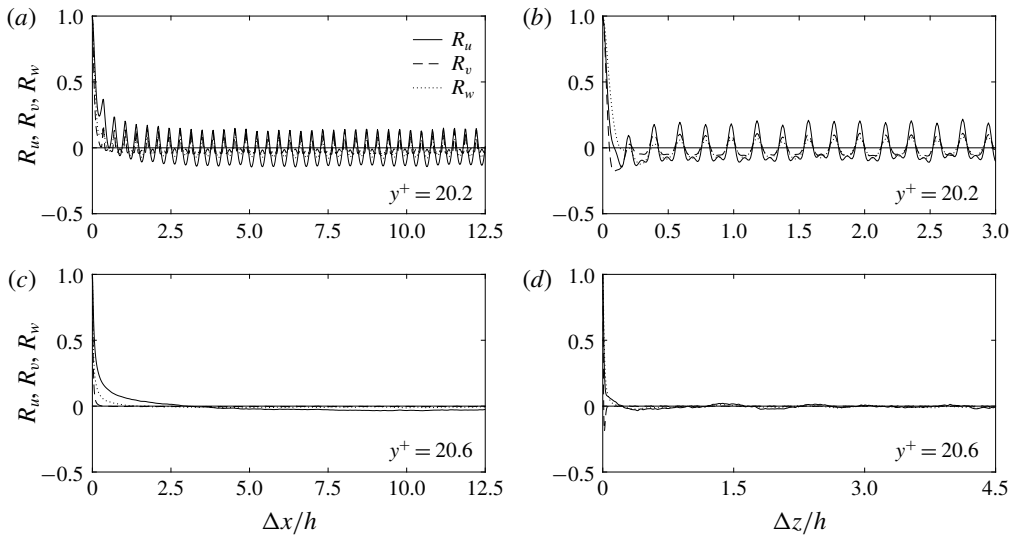
FIGURE 26. Two-point autocorrelation coefficients of velocity fluctuations for the smooth- and rough-wall cases at $y^+ = 20$. (*a,b*) RH400-20-4; (*c,d*) SM2000. Streamwise (left) and spanwise (right) profiles.
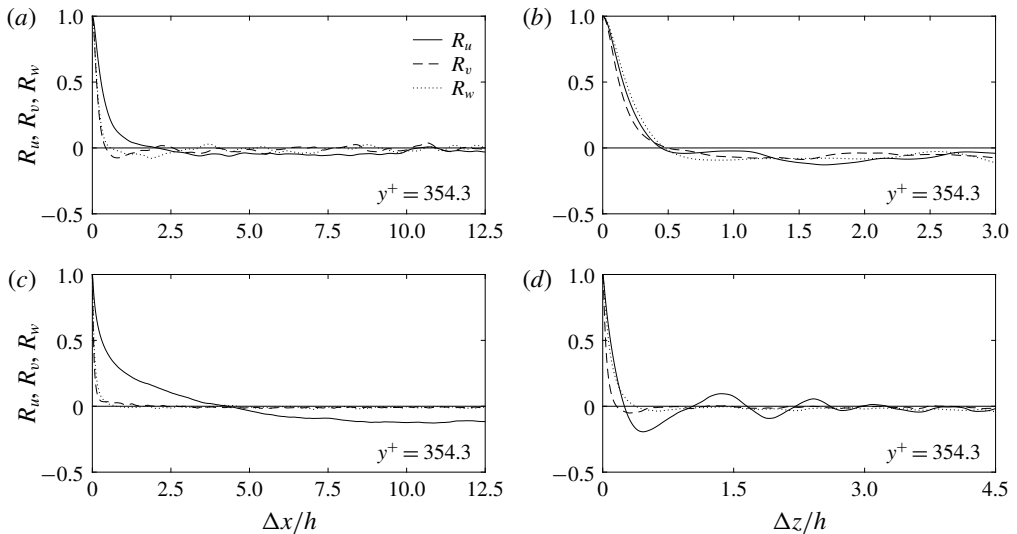

FIGURE 27. As in figure 26, but for $y^+ = 350$.

the roughness crest at $y^+ = 20$ exhibit periodic behaviour in both the streamwise and spanwise profiles, whose wavelength corresponds to the roughness-element spacings in the streamwise and spanwise directions, respectively. In contrast, the autocorrelation coefficients decay rapidly to zero in the smooth-wall case at $y^+ = 25$ as shown in figures 26(*c*) and 26(*d*). In the outer region at $y^+ = 350$, shown in figure 27, the autocorrelation coefficients for both cases decay to a value close to zero with
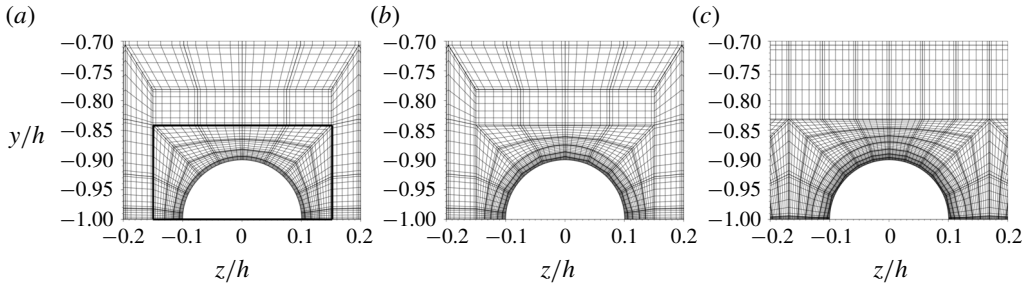
FIGURE 28. Mesh refinement around the hemispherical roughness for the rough-wall case at $Re_\tau = 300$ with $k/h = 0.1$ and $d/k = 4$. (*a*) Coarse (M3), 67, 584 grid points/cell; (*b*) moderate (M2), 215, 040 grid points/cell; (*c*) fine (M1), 387, 072 grid points/cell. Box in (*a*) denotes the boundary of the refined region (cell) enclosing each hemisphere.

increasing streamwise distance. Thus, these results support that the domain sizes are appropriate for the current simulations.

Appendix B. Mesh resolution

As indicated previously, the mesh above the roughness elements was selected according to the resolution used in previous DNS of smooth-wall flows at similar *Re* (Moser, Kim & Mansour 1999). The mesh around the hemispherical roughness were constructed using body-fitted spectral elements and the only reliable approach to determine its appropriateness was to conduct a mesh-refinement study in a dedicated set of simulations. A rough-wall turbulent channel flow at $Re_\tau = 300$ with $k/h = 0.1$ and $d/k = 4$ was used for this study and the different roughness cell meshes are shown in figure 28. The resolution of this mesh scales with wall units and can therefore be reliably used at other similar *Re*. As seen from figure 28(*a–c*), the mesh around the roughness elements was gradually refined in the streamwise, radial and spanwise directions, respectively. As a result, the number of grid points per roughness cell increased from 67 584 for the coarse mesh (M3), to 215 040 for the moderately refined mesh (M2) and to 387 072 for the fine mesh (M1), respectively, within the refined region. Note that outside the refined region, the mesh was constructed to ensure a smooth transition to the bulk of the computation mesh, as needed. The total number of grid points increases from $N3 = 193\,462\,272$ for M3, to $N2 = 533\,200\,896$ for M2 and to $N1 = 1\,242\,169\,344$ for M1, respectively. Therefore, the average grid refinement ratio is estimated to be $r = [(N2/N3)^{1/3} + (N1/N2)^{1/3}]/2 = 1.36$. Statistics were collected and averaged both temporally and spatially in the streamwise and spanwise directions at planes parallel to the wall for each mesh.

Figure 29 compares the Reynolds stress profiles for different mesh resolutions. In general, good agreements between these meshes are observed for all components of the Reynolds stresses, although there are small differences between the fine mesh and other two meshes in $\overline{u'^2}$ for $10 < y^+ < 30$ due to small geometrical deviations within the roughness sublayer. Despite these small deviations, the statistics obtained by the coarse mesh are nearly indistinguishable from those for the refined meshes. The grid convergence index (GCI) (Roache 1994) is also reported in table 4 and it is shown that the GCIs for all statistics are less than 2%, which is acceptable owing to the complex unstructured mesh studied herein. Given the large domain sizes and number of hemispheres considered in this study, the coarse mesh was used as a reference in
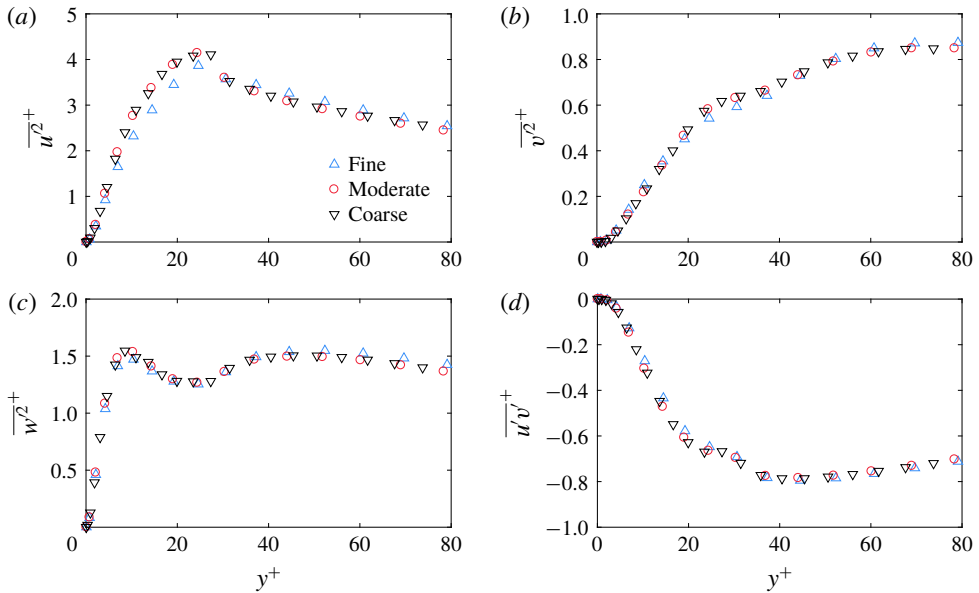
FIGURE 29. (Colour online) Comparison of the Reynolds stress for different mesh refinement schemes around the roughness elements at $Re_\tau = 300$ with $k/h = 0.1$ and $d/k = 4$.

Statistics	$|\epsilon_{31}|$	$|\epsilon_{21}|$	p	$GCI_{31}(\%)$	$GCI_{21}(\%)$
$\overline{u'^2}^+$	0.0225	0.0255	6.883	0.3762	0.4266
$\overline{v'^2}^+$	0.0626	0.0528	5.442	1.7724	1.4960
$\overline{w'^2}^+$	0.0059	0.0087	3.647	0.3512	0.5184
$\overline{u'v'}^+$	0.0023	0.0070	1.246	0.5971	1.8616

TABLE 4. Grid convergence parameters. $\epsilon_{i,j} = (f_i - f_j)/f_j$ where f_i is the target statistics at $y^+ = 30$ (roughness crest) for mesh i ($i = 1$, 2 and 3); $p = \ln(\epsilon_{21}/\epsilon_{32})/\ln(r)$ is the order of convergence, with the grid refinement ratio $r = 1.36$; $GCI_{i,j} = F_s|\epsilon_{i,j}|/(r^p - 1)$ is the grid convergence index with the safety factor $F_s = 1.25$.

designing and constructing all meshes used in the simulations presented herein (scaled in terms of appropriate wall units for each simulation).

Appendix C. Comparison of the extended original models

While the predictive model originally proposed by Mathis *et al.* (2011) exclusively focused on predictions involving u', several studies have attempted to extend the model to the other velocity components. In the present study, we proposed and made predictions of all three velocity components using simply the outer large-scale signal u', i.e. the 'single-large-scale' model. Alternatively, following Yin *et al.* (2018), we tested a model that calibrates the modulation constants and the universal signals using just u'^+_{OL} for all three velocity components but determines the superposition
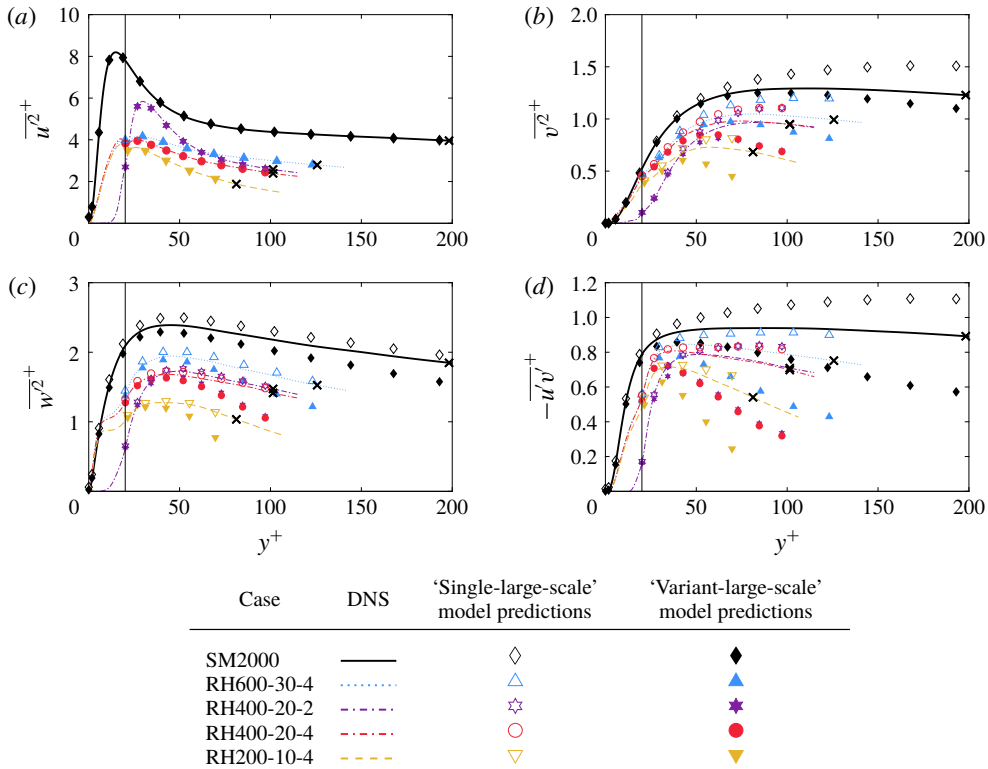
FIGURE 30. (Colour online) Predictions of the Reynolds stresses for the smooth- and rough-wall cases compared with the actual statistics from DNS. For the predictions involving v' and w', the modulation coefficients are still produced by u'^+_{OL} but the superposition constants are produced by either u'^+_{OL} ('single-large-scale' model; open symbols) or v'^+_{OL} and w'^+_{OL} ('variant-large-scale' model; filled symbols). Symbol $\times$ marks the reference location where the large-scale signal is extracted. Vertical lines denote the location of the roughness crest $k^+ = 20$.

constants based on the corresponding outer large-scale signals. For example, the superposition for v' is produced by v'^+_{OL} and the same applies for w'. This model is referred to herein as the 'variant-large-scale' model. Note that this model calibrates the universal signals using the same iterative method as the original model, which differs from the model by Yin *et al.* (2018) where the universal signals were replaced by the DNS data simulated using a minimal flow unit.

The predictions of the Reynolds stresses based on the two models are shown in figure 30 in comparison with the actual statistics from the DNS. As expected, both models perform equally well for $\overline{u'^2}$. The 'variant-large-scale' model yields better predictions for $\overline{v'^2}$ at higher *Re* but introduces large errors at lower *Re*. However, the 'single-large-scale' model produces more accurate and consistent predictions for $\overline{w'^2}$. Not surprisingly, both models generate significant errors when attempting to predict the Reynolds shear stress $\overline{u'v'}$ as neither of the models are able to fully capture the correlation between u' and v'. Several higher-order statistics are also compared as shown in figure 31. Overall, the 'variant-large-scale' model demonstrates improved
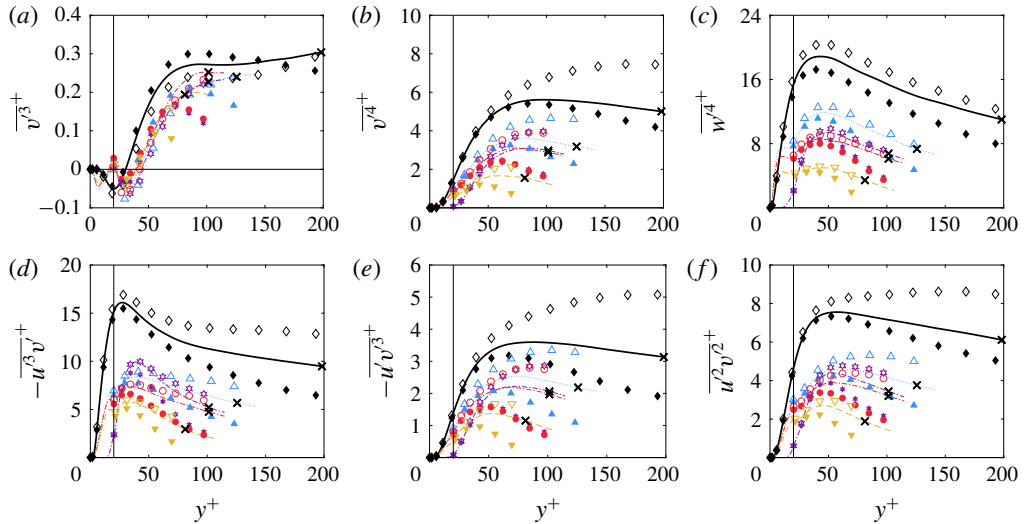
FIGURE 31. (Colour online) As in figure 30, but for the higher-order statistics.

predictions for statistics involving v' only at higher Re but the statistics for w' are better produced by the 'single-large-scale' model. Similar to $\overline{u'v'}$, both models fail to produce reliable predictions for the cross-product terms.

REFERENCES

ADRIAN, R. J. 2007 Hairpin vortex organization in wall turbulence. *Phys. Fluids* **19** (4), 041301.

AGOSTINI, L. & LESCHZINER, M. 2016 Predicting the response of small-scale near-wall turbulence to large-scale outer motions. *Phys. Fluids* **28** (1), 015107.

ANDERSON, W. 2016 Amplitude modulation of streamwise velocity fluctuations in the roughness sublayer: evidence from large-eddy simulations. *J. Fluid Mech.* **789**, 567–588.

ANDERSON, W., BARROS, J. M. & CHRISTENSEN, K. T. 2015 Numerical and experimental study of mechanisms responsible for turbulent secondary flows in boundary layer flows over spanwise heterogeneous roughness. *J. Fluid Mech.* **748**, 316–347.

ASHRAFIAN, A., ANDERSSON, H. I. & MANHART, M. 2004 DNS of turbulent flow in a rod-roughened channel. *Intl J. Heat Fluid Flow* **25** (3), 373–383.

BAILON-CUBA, J., LEONARDI, S. & CASTILLO, L. 2009 Turbulent channel flow with 2d wedges of random height on one wall. *Intl J. Heat Fluid Flow* **30** (5), 1007–1015.

BALAKUMAR, B. J. & ADRIAN, R. J. 2007 Large-and very-large-scale motions in channel and boundary-layer flows. *Phil. Trans. R. Soc. Lond.* A **365** (1852), 665–681.

BARROS, J. M. & CHRISTENSEN, K. T. 2014 Observations of turbulent secondary flows in a rough-wall boundary layer. *J. Fluid Mech.* **748**, R1.

BERNARDINI, M. & PIROZZOLI, S. 2011 Inner/outer interactions in turbulent boundary layers: a refined measure for the large-scale amplitude modulation mechanism. *Phys. Fluids* **23**, 061701.

BIRCH, D. M. & MORRISON, J. F. 2011 Similarity of the streamwise velocity component in very-rough-wall channel flow. *J. Fluid Mech.* **668**, 174–201.

BONS, J. P., TAYLOR, R. P., MCCLAIN, S. T. & RIVIR, R. B. 2001 The many faces of turbine surface roughness. In *ASME Turbo Expo 2001: Power for Land, Sea, and Air*, pp. V003T01A042–V003T01A042. American Society of Mechanical Engineers.

BRAGG, M. B., BROEREN, A. P. & BLUMENTHAL, L. A. 2005 Iced-airfoil aerodynamics. *Prog. Aerosp. Sci.* **41** (5), 323–362.

BURATTINI, P., LEONARDI, S. & ORLANDI, P. A. 2008 Comparison between experiments and direct numerical simulations in a channel flow with roughness on one wall. *J. Fluid Mech.* **600**, 403–426.

BUSSE, A., LUTZNER, M. & SANDHAM, N. D. 2015 Direct numerical simulation of turbulent flow over a rough surface based on a surface scan. *Comput. Fluids* **116**, 129–147.

BUSSE, A., THAKKAR, M. & SANDHAM, N. D. 2017 Reynolds-number dependence of the near-wall flow over irregular rough surfaces. *J. Fluid Mech.* **810**, 196–224.

CHAN-BRAUN, C., GARCÍA-VILLALBA, M. & UHLMANN, M. 2011 Force and torque acting on particles in a transitionally rough open-channel flow. *J. Fluid Mech.* **684**, 441–474.

CHATZIKYRIAKOU, D., BUONGIORNO, J., CAVIEZEL, D. & LAKEHAL, D. 2015 DNS and LES of turbulent flow in a closed channel featuring a pattern of hemispherical roughness elements. *Intl J. Heat Fluid Flow* **53**, 29–43.

CHENG, H. & CASTRO, I. P. 2002 Near wall flow over urban-like roughness. *Boundary-Layer Meteorol.* **104** (2), 229–259.

CHOI, H., MOIN, P. & KIM, J. 1993 Direct numerical simulation of turbulent flow over riblets. *J. Fluid Mech.* **255**, 503–539.

CHRISTENSEN, K. T. & ADRIAN, R. J. 2001 Statistical evidence of hairpin vortex packets in wall turbulence. *J. Fluid Mech.* **431**, 433–443.

CHU, D. C. & KARNIADAKIS, G. E. 1993 A direct numerical simulation of laminar and turbulent flow over riblet-mounted surfaces. *J. Fluid Mech.* **250**, 1–42.

COCEAL, O., DOBRE, A., THOMAS, T. G. & BELCHER, S. E. 2007 Structure of turbulent flow over regular arrays of cubical roughness. *J. Fluid Mech.* **589**, 375–409.

COLEBROOK, C. F. & WHITE, C. M. 1937 Experiments with fluid friction in roughened pipes. *Proc. R. Soc. Lond.* A **161** (906), 367–381.

DE ANGELIS, V., LOMBARDI, P. & BANERJEE, S. 1997 Direct numerical simulation of turbulent flow over a wavy wall. *Phys. Fluids* **9** (8), 2429–2442.

FINNIGAN, J. 2000 Turbulence in plant canopies. *Annu. Rev. Fluid Mech.* **32** (1), 519–571.

FISCHER, P. F. 2010 nek tutorial. http://www.mcs.anl.gov/~fischer/nek5000/.

FISCHER, P. F., LOTTES, J. W. & KERKEMEIER, S. G. 2014 nek5000 Web page. https://nek5000.mcs.anl.gov/.

FLACK, K. A., SCHULTZ, M. P. & CONNELLY, J. S. 2007 Examination of a critical roughness height for outer layer similarity. *Phys. Fluids* **19** (9), 095104.

FLACK, K. A., SCHULTZ, M. P. & SHAPIRO, T. A. 2005 Experimental support for Townsend's Reynolds number similarity hypothesis on rough walls. *Phys. Fluids* **17** (3), 035102.

GANAPATHISUBRAMANI, B., HUTCHINS, N., HAMBLETON, W. T., LONGMIRE, E. K. & MARUSIC, I. 2005 Investigation of large-scale coherence in a turbulent boundary layer using two-point correlations. *J. Fluid Mech.* **524**, 57–80.

GANAPATHISUBRAMANI, B., LONGMIRE, E. K. & MARUSIC, I. 2003 Characteristics of vortex packets in turbulent boundary layers. *J. Fluid Mech.* **478**, 35–46.

GHODKE, C. D. & APTE, S. V. 2016 Dns study of particle-bed–turbulence interactions in an oscillatory wall-bounded flow. *J. Fluid Mech.* **792**, 232–251.

HONG, J., KATZ, J. & SCHULTZ, M. P. 2011 Near-wall turbulence statistics and flow structures over three-dimensional roughness in a turbulent channel flow. *J. Fluid Mech.* **667**, 1–37.

HOYAS, S. & JIMÉNEZ, J. 2006 Scaling of the velocity fluctuations in turbulent channels up to $Re_\tau = 2003$. *Phys. Fluids* **18** (1), 011702.

HOYAS, S. & JIMÉNEZ, J. 2008 Reynolds number effects on the Reynolds-stress budgets in turbulent channels. *Phys. Fluids* **20** (10), 101511.

HUTCHINS, N. & MARUSIC, I. 2007a Evidence of very long meandering features in the logarithmic region of turbulent boundary layers. *J. Fluid Mech.* **579**, 1–28.

HUTCHINS, N. & MARUSIC, I. 2007b Large-scale influences in near-wall turbulence. *Phil. Trans. R. Soc. Lond.* A **365** (1852), 647–664.

IKEDA, T. & DURBIN, P. A. 2007 Direct simulations of a rough-wall channel flow. *J. Fluid Mech.* **571**, 235–263.

JIMÉNEZ, J. 2004 Turbulent flows over rough walls. *Annu. Rev. Fluid Mech.* **36**, 173–196.

JIMÉNEZ, J. & HOYAS, S. 2008 Turbulent fluctuations above the buffer layer of wall-bounded flows. *J. Fluid Mech.* **611**, 215–236.

JIMÉNEZ, J. & MOIN, P. 1991 The minimal flow unit in near-wall turbulence. *J. Fluid Mech.* **225**, 213–240.

JOHNSON, R. A. & WICHERN, D. W. 2014 *Applied Multivariate Statistical Analysis*. Prentice-Hall.

KIM, J., MOIN, P. & MOSER, R. 1987 Turbulence statistics in fully developed channel flow at low Reynolds number. *J. Fluid Mech.* **177**, 133–166.

KIM, K. C. & ADRIAN, R. J. 1999 Very large-scale motion in the outer layer. *Phys. Fluids* **11**, 417–422.

KROGSTAD, P.-Å., ANDERSSON, H. I., BAKKEN, O. M. & ASHRAFIAN, A. 2005 An experimental and numerical study of channel flow with rough walls. *J. Fluid Mech.* **530**, 327–352.

LEE, J.-H., SUNG, H.-J. & KROGSTAD, P.-A. 2011 Direct numerical simulation of the turbulent boundary layer over a cube-roughened wall. *J. Fluid Mech.* **669**, 397–431.

LEE, M. & MOSER, R. D. 2015 Direct numerical simulation of turbulent channel flow up to. *J. Fluid Mech.* **774**, 395–415.

LEE, S.-H. & SUNG, H.-J. 2007 Direct numerical simulation of the turbulent boundary layer over a rod-roughened wall. *J. Fluid Mech.* **584**, 125–146.

LEONARDI, S. & CASTRO, I. P. 2010 Channel flow over large cube roughness: a direct numerical simulation study. *J. Fluid Mech.* **651**, 519–539.

MARUSIC, I., MATHIS, R. & HUTCHINS, N. 2010 Predictive model for wall-bounded turbulent flow. *Science* **329** (5988), 193–196.

MATHIS, R., HUTCHINS, N. & MARUSIC, I. 2009*a* Large-scale amplitude modulation of the small-scale structures in turbulent boundary layers. *J. Fluid Mech.* **628**, 311–337.

MATHIS, R., HUTCHINS, N. & MARUSIC, I. 2011 A predictive inner–outer model for streamwise turbulence statistics in wall-bounded flows. *J. Fluid Mech.* **681**, 537–566.

MATHIS, R., MARUSIC, I., CHERNYSHENKO, S. I. & HUTCHINS, N. 2013 Estimating wall-shear-stress fluctuations given an outer region input. *J. Fluid Mech.* **715**, 163–180.

MATHIS, R., MONTY, J. P., HUTCHINS, N. & MARUSIC, I. 2009*b* Comparison of large-scale amplitude modulation in turbulent boundary layers, pipes, and channel flows. *Phys. Fluids* **21** (11), 111703.

MEJIA-ALVAREZ, R. & CHRISTENSEN, K. T. 2013 Wall-parallel stereo particle-image velocimetry measurements in the roughness sublayer of turbulent flow overlying highly irregular roughness. *Phys. Fluids* **25** (11), 115109.

MEJIA-ALVAREZ, R. & CHRISTENSEN, K. T. 2010 Low-order representations of irregular surface roughness and their impact on a turbulent boundary layer. *Phys. Fluids* **22** (1), 015106.

MEJIA-ALVAREZ, R., WU, Y. & CHRISTENSEN, K. T. 2014 Observations of meandering superstructures in the roughness sublayer of a turbulent boundary layer. *Intl J. Heat Fluid Flow* **48**, 43–51.

MONIN, A. S. 1970 The atmospheric boundary layer. *Annu. Rev. Fluid Mech.* **2** (1), 225–250.

MOSER, R. D., KIM, J. & MANSOUR, N. N. 1999 Direct numerical simulation of turbulent channel flow up to $Re_\tau = 590$. *Phys. Fluids* **11** (4), 943–945.

NAGANO, Y., HATTORI, H. & HOURA, T. 2004 DNS of velocity and thermal fields in turbulent channel flow with transverse-rib roughness. *Intl J. Heat Fluid Flow* **25** (3), 393–403.

NIKURADSE, J. 1933 Laws of flow in rough pipes. *VDI Forschungsheft*. Citeseer.

ORLANDI, P. & LEONARDI, S. 2008 Direct numerical simulation of three-dimensional turbulent rough channels: parameterization and flow physics. *J. Fluid Mech.* **606**, 399–415.

ORLANDI, P., LEONARDI, S. & ANTONIA, R. A. 2006 Turbulent channel flow with either transverse or longitudinal roughness elements on one wall. *J. Fluid Mech.* **561**, 279–305.

PATHIKONDA, G. & CHRISTENSEN, K. T. 2017*a* Inner–outer interactions in a turbulent boundary layer overlying complex roughness. *Phys. Rev. Fluids* **2**, 044603.

PATHIKONDA, G. & CHRISTENSEN, K. T. 2017*b* Investigation of inner-outer interactions in a turbulent boundary layer using time-resolved PIV. In *10th Intl Symposium on Turbulence and Shear Flow Phenomena (TSFP10)*.

PERRY, A. E., SCHOFIELD, W. H. & JOUBERT, P. N. 1969 Rough wall turbulent boundary layers. *J. Fluid Mech.* **37** (02), 383–413.

RAUPACH, M. R., ANTONIA, R. A. & RAJAGOPALAN, S. 1991 Rough-wall turbulent boundary layers. *Appl. Mech. Rev.* **44** (1), 1–25.

ROACHE, P. J. 1994 Perspective: a method for uniform reporting of grid refinement studies. *Trans. ASME J. Fluids Engng* **116** (3), 405–413.

SCOTTI, A. 2006 Direct numerical simulation of turbulent channel flows with boundary roughened with virtual sandpaper. *Phys. Fluids* **18** (3), 031701.

SIROVICH, L. 1987 Turbulence and the dynamics of coherent structures part I: coherent structures. *Q. Appl. Maths* **45** (3), 561–571.

SQUIRE, D. T., BAARS, W. J., HUTCHINS, N. & MARUSIC, I. 2016 Inner–outer interactions in rough-wall turbulence. *J. Turbul.* **17** (12), 1159–1178.

TALLURU, K. M., BAIDYA, R., HUTCHINS, N. & MARUSIC, I. 2014 Amplitude modulation of all three velocity components in turbulent boundary layers. *J. Fluid Mech.* **746**, R1.

TOMKINS, C. D. & ADRIAN, R. J. 2003 Spanwise structure and scale growth in turbulent boundary layers. *J. Fluid Mech.* **490**, 37–74.

TOWNSEND, A. A. 1976 *The Structure of Turbulent Shear Flow*. Cambridge University Press.

VIGNOLES, G. L., LACHAUD, J., ASPA, Y. & GOYHÉNÈCHE, J. 2009 Ablation of carbon-based materials: multiscale roughness modelling. *Compos. Sci. Technol.* **69** (9), 1470–1477.

VOLINO, R. J., SCHULTZ, M. P. & FLACK, K. A. 2007 Turbulence structure in rough- and smooth-wall boundary layers. *J. Fluid Mech.* **592**, 263–293.

WILLINGHAM, D., ANDERSON, W., CHRISTENSEN, K. T. & BARROS, J. M. 2014 Turbulent boundary layer flow over transverse aerodynamic roughness transitions: Induced mixing and flow characterization. *Phys. Fluids* **26** (2), 025111.

WU, Y. & CHRISTENSEN, K. T. 2007 Outer-layer similarity in the presence of a practical rough-wall topography. *Phys. Fluids* **19** (8), 085108.

WU, Y. & CHRISTENSEN, K. T. 2010 Spatial structure of a turbulent boundary layer with irregular surface roughness. *J. Fluid Mech.* **655**, 380–418.

YIN, G., HUANG, W.-X. & XU, C.-X. 2018 Prediction of near-wall turbulence using minimal flow unit. *J. Fluid Mech.* **841**, 654–673.

YUAN, J. & PIOMELLI, U. 2014 Roughness effects on the Reynolds stress budgets in near-wall turbulence. *J. Fluid Mech.* **760**, R1.